Institut für Geodäsie und Geoinformation

Professur für Astronomische, Physikalische und Mathematische Geodäsie

Implementing real-time water level retrieval for GNSS interferometric reflectometry

MASTER THESIS

by

Alonso Vega-Fernández

BONN, 2023

SUPERVISORS:

EMERITA PROF.- DR. KRISTINE M. LARSON

DR. MAKAN A. KAREGAR

UNIVERSITÄT BONN

igg

Rheinische
Friedrich-Wilhelms-
Universität Bonn

Institut für Geodäsie und
Geoinformation

Emerita Prof. Kristine M. Larson

53115 Bonn
Nussallee 17
kusche@uni-bonn.de

Sekretariat: C. van Eckeren
Tel.: +49(0)228/73-2628
Fax: +49(0)228/73-3029
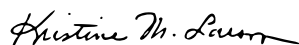vaneckeren@uni-bonn.de
www.igg.uni-bonn.de

Bonn, 01.07.2022

**M.Sc. Geodetic Engineering
Master thesis Task**

„Implementing real-time water level retrieval for GNSS interferometric reflectometry "

for Alonso Vega Fernandez

GNSS interferometric reflectometry has shown its potential for widespread use in environmental monitoring. Water level, snow accumulation, among others, are now routinely computed from receiver-generated signal-to-noise ratio (SNR) data. Each satellite track's SNR measurements can be analyzed using spectral analysis methods such as the Lomb Scargle Periodogram (LSP) to determine the peak SNR frequency and corresponding reflector height. However, depending on the site, the LSP method requires from 20-60 minutes of data to retrieve an individual reflector height. This is a limiting factor for real-time retrievals of water level in natural hazard identification and warning system application. Kalman filtering has been recently suggested as an effective method for both inverting SNR data from multiple arcs and estimating water levels in real-time. In this thesis, SNR data collected from a coastal site and a river site are analyzed using the *gnssrefl* python software package. This software is currently capable of measuring reflector heights using either spectral techniques or inversion but is restricted to non-real time applications. The student will extend from available python libraries to (1) enhance the use of the software for real-time application, (2) to thoroughly assess the performance of the Kalman filter approach for sea-level estimation at a coastal site and a river site.

Kristine M. Larson, Makan Karegar

Affirmation

I herewith declare that I have independently written this thesis. Only the sources cited have been used in this work. Parts that are direct quotes or paraphrases are identified as such.

Bonn, February, 15th 2023

_____

(Alonso Vega-Fernández)

Acknowledgements

Abstract

The technique of measuring and tracking water levels in order to spot trends and patterns in water levels is known as water surface-level monitoring. Real-time monitoring enables the fast and precise collection of information that may then be utilized to guide emergency response and decision-making processes.

Various methods and high-tech equipment can be used to conduct real-time observations. However, the installation of these devices is frequently limited to locations inside or adjacent to water bodies, where the instruments are vulnerable to damage during intense events and could fail to transmit data at crucial times. Therefore, alternative non-intrusive techniques such as ground-based GNSS Interferometric Reflectometry (GNSS-IR), which do not require equipment in vulnerable structures, should be prioritized. For that reason, this research aims to develop a real-time GNSS-IR implementation using a Kalman filter in order to create a tool compatible with the python package *gnssrefl* capable of monitoring water levels both at the sea surface and in rivers.

The Ensemble Kalman filter (EnKF) was used to design the implementation. This filter uses a collection of system states in the prediction and update process to estimate the most likely state and its variance. Signal-to-noise ratio (SNR) data measured by Global Navigation Satellite System (GNSS) devices positioned at places that guarantee the reception of signals reflected by the water surface are used as input observations in the update stage. The estimated water levels were compared to tide or river gauge records to determine the accuracy of the results.

The results demonstrated that the developed implementation can monitor sea level in real-time utilizing GNSS antenna measurements that capture multiple constellations and frequencies, with RMSE of 4.2 *cm*. However, the performance of the filter was limited when facing extreme conditions where the roughness of the water surface does not allow specular reflections. In the case of real-time river level monitoring, it was demonstrated that the implementation can draw river dynamics even in the presence of flooding, obtaining RMSE of 3.7 *cm*. The use of low-cost devices capable of measuring only the GPS signal at L1 frequency was explored in river monitoring, finding that it is possible to obtain RMSE values of 3.0 *cm* or less when the instrument is installed pointing towards the horizon in the direction of the river.

Contents

Appendices xvii

Chapter 1

Introduction

Water surface-level change monitoring is the process of systematic measurement and tracking of the level of water bodies such as rivers, lakes, and oceans. It is an important aspect of environmental and water resource management, as it allows the identification of trends and patterns in water levels and helps to predict and mitigate the potential impacts of flooding and drought. It is necessary for industries such as agriculture, energy production, and shipping, which rely on a stable and predictable water supply. Accurate water level monitoring allows the proper management of water resources and the efficient use of water for irrigation, hydroelectric power generation, and navigation. It is crucial for flood prevention and warning systems as well.

Historically, human settlement patterns and social structures have been affected by access to water. Nowadays, about 10% of the world's population resides in coastal areas, where some of the world's largest cities are located, while another large percentage has settled in regions surrounding rivers and lakes. Thus, there is a close relationship between various human activities and water bodies, but at the same time, these settlements are vulnerable to natural disasters and hazards (Neumann et al., 2015; Kirezci et al., 2020). By tracking changes in water level, communities can be alerted to potential flood risks and take the necessary precautions to protect lives and property. Additionally, the monitoring of water levels contributes to the preservation of sensitive ecosystems and recreational areas for the enjoyment of the public.

1.1   The importance of real-time monitoring of water level

Real-time monitoring of water levels allows timely and accurate information to be gathered and used to inform decision-making and emergency response efforts. This is especially critical in situations like heavy rainfall or rapid snow melt, where rapid changes in water level can have damaging consequences. By providing up-to-date data on water levels, real-time monitoring systems help to ensure the safety of communities, the protection of infrastructure, and the preservation of natural habitats.

In the case of coastal regions, multiple productive activities are required to have information in real-time. For example, real-time sea level determination is crucial in local and international trade since it is necessary in the operation of ports and marinas in order to guarantee that ships can maneuver without the danger of running aground due to low tides. Real-time sea level measurements also play a determining role in the detection of imminent threats. Coastal zones are characterized to have low elevation which makes them vulnerable to the effects of phenomena such as coastal flooding, which frequency has been amplified in the last decade by the sea level rise (Vitousek et al., 2017; Taherkhani et al., 2020).

Unforced climate variability and natural and anthropogenic forcing factors are inducing the global mean sea level to rise (Frederikse et al., 2020). Studies have shown that the global mean sea level has been rising over the past 100 years, and the rising rate has been increasing. During the period 1901 - 1971, the sea level rose 1.3 $mm\ yr^{-1}$ while from 2006 - 2018 it increased to 3.7 $mm\ yr^{-1}$ (Arias et al., 2021). The estimated sea level rise acceleration over the period 1993 - 2018 reached 0.1 $mm\ yr^{-2}$ (WCRP Global Sea Level Budget Group, 2018) indicating that the risk of potentially destructive events at the coastal regions is constantly increasing, giving even more importance to real-time sea level measurement systems for early warning and disaster prevention.

On the other hand, the inland water surface is a source of water for economic activities related to industry and agriculture, is often used as means for navigation and transport of merchandise materials, and in the production of hydroelectric power. Real-time inland water level measurements play an important role in hydrology and environmental sciences in a variety of interdisciplinary applications, as well as a critical tool for early warning to monitor the potential for inland flooding. Climate change has been related to the increase in the frequency of extreme events (Tabari, 2020) that can rapidly increase the rivers discharge, and therefore rising the water level, which can be potentially dangerous

for human settlements near the riverbed and can result in the destruction of properties, important infrastructure and even in the loss of human life.

Real-time water level observations can be carried out using a variety of techniques. Sensor technologies such as pressure transducers, shaft encoders, bubbler systems, non-contact RADAR systems, or acoustic sensors are used to make in–situ measurements in both coastal and inland water to record water surface changes. Significant advances in these techniques have been implemented in order to guarantee the acquisition and transfer of the information to capture temporal changes that occur during episodic events such as precipitation and major storm events (Younos & Heyer, 2015). However, the installation of these devices is often restricted to structures that generally need to be close or inside the water bodies (e.g. stilling well, mast, bridge), where the instruments are exposed to damage during extreme events, causing data transmission to stop working at critical moments. Therefore, the use of alternative non-intrusive methods that do not require instrumentation in vulnerable structures is a priority to ensure uninterrupted monitoring of the water level.

Remote sensing techniques, such as satellite altimetry, have been widely used to accurately monitor marine and inland water levels for more than 30 years, including technological advances in missions such as Surface Water and Ocean Topography (SWOT), that promise to be a tool that will enhance the monitoring of water bodies (Abdalla et al., 2021). However, the technical characteristics of this space technology, such as the repetition period or the time required for data processing, difficult this technique implementation in real time.

The ground-based GNSS - Interferometric Reflectometry (GNSS-IR) (Anderson, 2000) is an alternative remote sensing technique for water level monitoring that has been gaining popularity and its contributions are going to be detailed below.

1.2   The contribution of GNSS-IR to real-time water-level measurements

Global Navigation Satellite System (GNSS) is a conjunction of satellite constellations (e.g. GPS, GLONASS, Galileo) that transmit signals used to determine the location, speed, and time of on-ground devices. In geodesy, these signals are mainly used for positioning and navigation Ogaja (2022). However, in recent years the technique GNSS-IR has been

incorporated as an alternative in the determination of water surfaces levels by using GNSS reflected signal and has shown reliable results in sea level monitoring (Larson, Löfgren, & Haas, 2013; Strandberg et al., 2016; Peng et al., 2021), the study of ocean tides (Löfgren et al., 2014; Larson et al., 2017; Geremia-Nievinski et al., 2020; Xie et al., 2021), and coastal hazards (Peng et al., 2019; Kim & Park, 2021; Kim et al., 2021), as well as river and lakes level determination (Vu et al., 2018; Holden & Larson, 2021; Karegar et al., 2022) and promising results in near-real-time (Purnell, 2022; Liu et al., 2023) and real-time implementations of sea level monitoring (Strandberg et al., 2019).

Unlike other GNSS applications where it is required the GNSS antenna to be installed directly on the object being measured, GNSS-IR is based on Signal-to-Noise Ratio (SNR) data, which is an indicator of received signal strength as the ratio of the direct satellite signal and the reflected signal, allowing the antenna to operate from a moderate distance from the reflecting surface (e.g. sea, river), protecting the measurement instruments from storm surges and flooding events.

The main requirement for ground-based GNSS-IR is a GNSS receiver with a clear line-of-sight to a sensing zone in the water surface from which the reflected satellite signal can be detected by the antenna (discussed in more detail later). This allows any existing GNSS antenna that meets this requirement could be used for water level monitoring. Making it possible to use these structures without the need for extra economic cost. Likewise, low-cost instruments have also proven to be efficient in obtaining data for water level monitoring (Williams et al., 2020; Fagundes et al., 2021; Karegar et al., 2022), allowing the implementation of GNSS-IR without the need for high economic investments.

1.3 Principle of GNSS-IR for water-level measurement

The GNSS antennas are instruments capable of receiving satellite signals from the Global Navigation Satellite Systems (e.g. GPS, GLONASS, Galileo, and BeiDou) and are used in applications such as positioning, navigation, and time determination (Ogaja, 2022). In geodesy, they are often used to determine land motion, allowing to monitor deformations of the earth's crust or control of coastal movements, for instance, controlling vertical displacements of tide gauges.

In the GNSS measurements the directly received satellite signal is affected by other ver-

sions of the signal that is reflected off surrounding surfaces, this is known as the multipath error. The presence of this error is measured by the receiver as SNR, that is the strength of the received signal and the noise density. In most GNSS geodetic implementations, the SNR is considered an indicator of the signal quality. However, it can also be used to obtain some information on the reflecting surfaces (Bilich & Larson, 2007; Nievinski & Larson, 2013). This idea is the base of GNSS-IR.
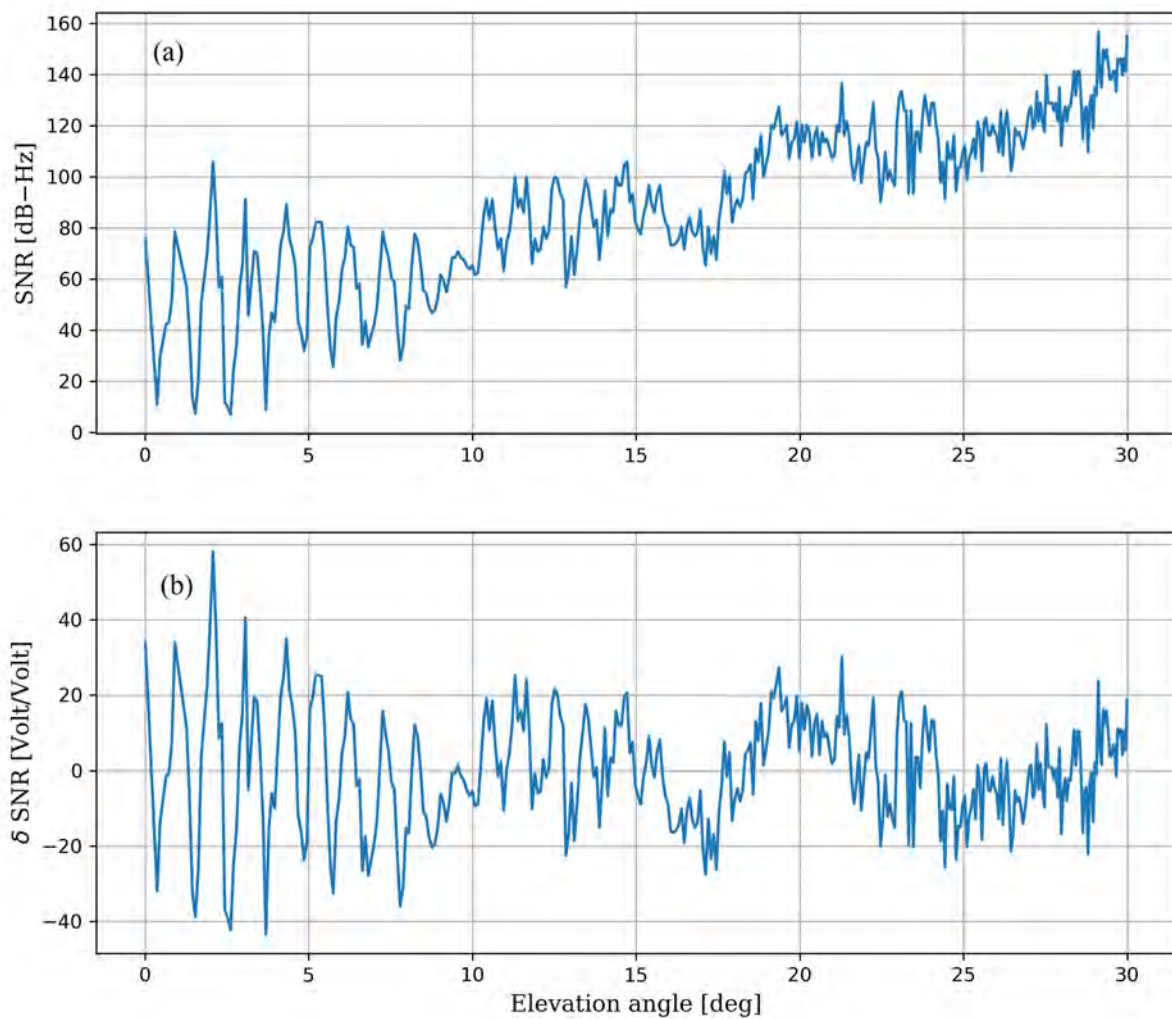
Figure 1.3.0.1: SNR signal strength for the L2 signal from GPS satellite G25 recorded at the station TGMX in Puerto Morelos, Mexico, February 12th, 2022. (a) Signal as recorded by the receiver. (b) Oscillating part of the signal, detrended with a 2nd order polynomial and converted to linear units.

The ground-based GNSS-IR was first introduced by Anderson (2000) and has been widely explored in multiple applications. This technique consists of the analysis of interference patterns by using the SNR proportional to the signal composite power P_c (i.e. $SNR = P_c$). As deduced from Georgiadou & Kleusberg (1988) and Nievinski & Larson (2013), the

composite power of the direct and the reflected signals can be defined by

$$SNR = P_d + P_r + 2\sqrt{P_r P_d} \cos \phi \qquad (1.1)$$

where P_d and P_r are the direct and reflected signal power respectively, and ϕ is the phase delay between the two signals.

As shown in Figure 1.3.0.1 (a), the strength of SNR varies with the elevation angle of the satellite emitting the signal. This is explained by the change in ϕ between the direct and reflected signal that occurs as a response to the change in the reflection angle while the satellite moves along its orbit. As a result, the direct and reflected signals are in phase or out of phase from time to time, increasing and decreasing the signal strength respectively.
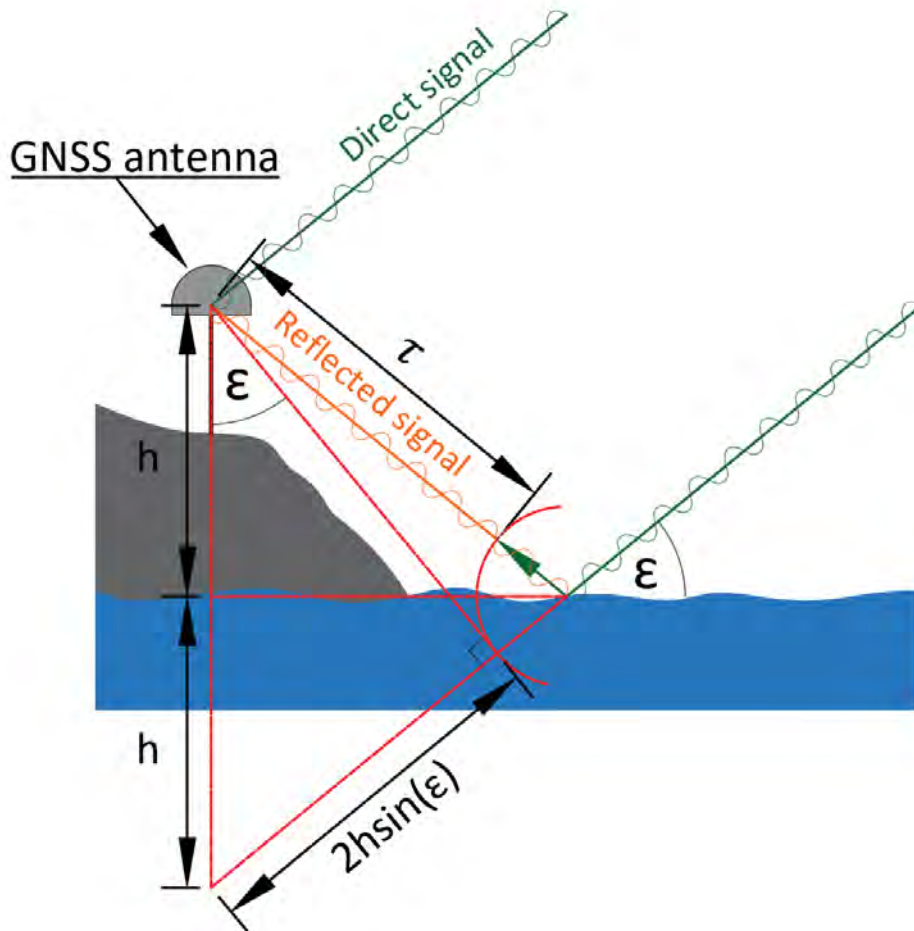
Figure 1.3.0.2: Diagram of ground-based GNSS-IR principle to monitoring water with a single GNSS antenna. The receiver measures the interference between the direct (green) and the reflected (orange) signals. Signals are reflected from an assumed planar water surface with the same elevation angle the satellites have with respect to the antenna phase center.

The trigonometry of the signals path can be explained based on Figure 1.3.0.2 by making

some assumptions to simplify the interpretation of the direct and reflected path length difference. First, since the distance between the GNSS satellite and the receiver is very large (e.g. > 20000 km), the signals path can be considered parallel before the signal is reflected, and second, the reflected surface is horizontal and planar, that is a good assumption for local water bodies surfaces (i.e. sea, lakes, rivers). As can be inferred from the shown signal trajectories, the reflected signal always travels a longer distance to achieve the antenna phase center than the direct signal. This extra distance τ is described by

$$\tau = 2h\sin(\epsilon) \tag{1.2}$$

where h is the vertical distance (i.e. height) of the reflective surface with respect to the phase center of the receiver, and ϵ is the satellite elevation angle. Thus, the phase delay ϕ will depend on the extra distance τ and the wavelength λ of the signal, and can be written as

$$\phi = \frac{4\pi}{\lambda}\tau \tag{1.3}$$

By substituting Equation 1.2 into 1.3 it is clear that the signal delay is dependent on the satellite elevation angle

$$\phi = \frac{2\pi h}{\lambda}\sin(\epsilon) + \varphi \tag{1.4}$$

where φ represents material properties of the reflective surface that can cause additional non-geometric phase offset. By combining Equations 1.1 and 1.4, it is possible to establish that the SNR contains information about the reflective surface. Therefore, h can be determined from the observed SNR.

The reflector height, h, can be retrieved from the SNR by implementing two different methods. The Spectral Analysis method (Larson, Löfgren, & Haas, 2013) and the Least Squares Inversion method (Strandberg et al., 2016).

1.3.1   Spectral analysis method

Spectral analysis is a technique that consists of the study of an oscillating signal to determine the frequencies present in it. In the case of GNSS-IR, the spectral analysis method studies the oscillating pattern drawn by the SNR to determine the dominant frequency f and uses it to retrieve the height of the reflective surface. Since the GNSS antenna is measuring signals from many satellites at the same time, the data have to separate into individual arcs, that consist of all the consecutive measurements from an individual satellite and frequency during the time it is observed by the receiver. The arcs are arranged by elevation angle, thus they can also be separated into ascending and

descending parts of the measurements from an individual arc. Figure 1.3.0.1 (a) shows the SNR between the elevation angles 0° to 30° depicted as a multi-path interference superimposed to an overall trend.

To start with the method implementation, the SNR has to be converted from units of $dB - Hz$ to a linear scale of units $Volt/Volt$ (assuming a 1Hz bandwidth) by using

$$SNR_L = 10^{SNR/20} \tag{1.5}$$

The SNR_L of the individual satellite arcs is separated into two components. The trend component SNR_t accounts for the long-period variation caused by the changing distance between the receiver and the satellite, and δSNR, which describes the oscillating part of Equation 1.1. Only the second aforementioned component contains information about the reflective surface. Therefore, the trend component is approximated using a low degree polynomial (e.g. 2nd order) and removed, e.i.

$$\delta SNR = SNR_L - SNR_t \tag{1.6}$$

to focus only on the information carried in the oscillating component (Figure 1.3.0.1 (b)). Thus, δSNR can be written proportional to

$$\delta SNR = A \cos \left[\frac{4\pi h}{\lambda} \sin(\epsilon) + \varphi \right] \tag{1.7}$$

where A is the amplitude of the oscillations (Nievinski & Larson, 2013), e.i. equivalent to $2\sqrt{P_r P_d}$. Moreover, considering δSNR as a sine wave function of $\sin(\epsilon)$, and h constant, the frequency f of the signal can be described by (Larson et al., 2007)

$$f = \frac{2h}{\lambda} \tag{1.8}$$

Therefore, it is possible to retrieve information about the reflective surface height with respect to the receiver by analyzing the spectrum of the signal. The Lomb-Scargle periodogram (LSP) method is usually used due to the SNR data is not regularly sampled in $\sin(\epsilon)$. By implementing the LSP analysis and the Equation 1.8, the dominant frequency (e.i. peak of the periodogram) of each satellite arc can be transformed to reflector heights. An example is shown in Figure 1.3.1.1, where a height of 12.599 m is retrieved by finding the peak of the LSP periodogram of the δSNR signal of one GPS L2 arc.

The assumption of a static reflective surface is valid for water level only when it can be considered relatively stationary during a satellite pass. However, when retrieving water level on a dynamic surface with large variations the actual surface position varies while a

satellite is observed, and the aforementioned assumption is no longer meaningful. In this case, the retrieved height has to be corrected by the change range (Larson, Ray, et al., 2013), expressing the frequency by

$$f = \frac{2}{\lambda} \left[h + \frac{\dot{h}\tan(\epsilon)}{\dot{\epsilon}} \right] \tag{1.9}$$

where $\dot{h}$ represents the height range of change and $\dot{\epsilon}$ the change in the elevation angle.
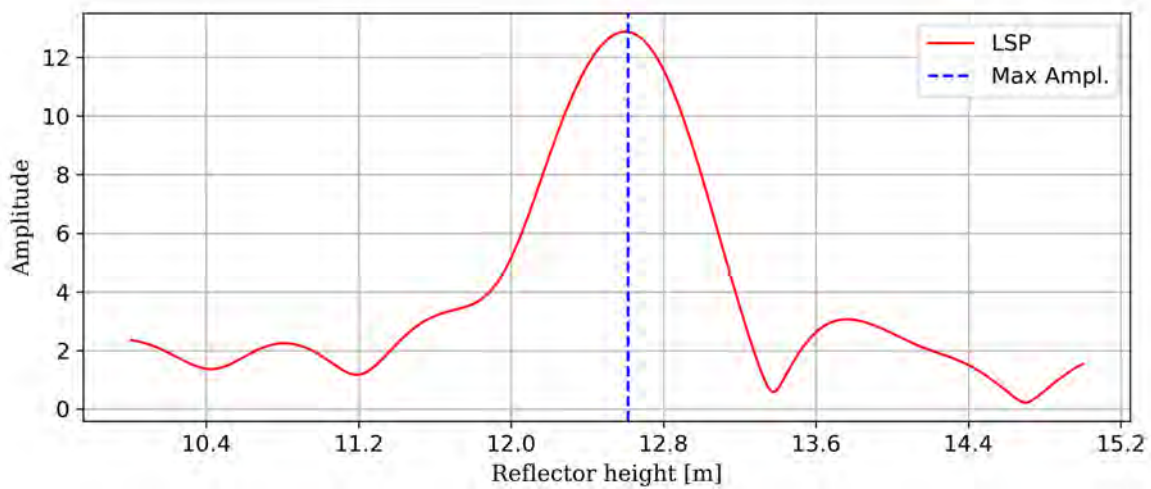

Figure 1.3.1.1: Lomb-Scargle power spectra from GPS L2 signal (satellite 15) measured at station GWES (GWES00DEU) in the Rhine river in Wesel, Germany, on July 2nd, 2021. The red curve represents the power spectra. The maximum amplitude of the curve is marked with a vertical blue dashed line, which also indicates the height of the reflective surface with respect to the GNSS antenna (12.599 m).

This method can be used to estimate water level near real-time since it typically requires 20–60 min to retrieve a reflector height. The time necessary to estimate h mainly depends on the used azimuth-elevation angle mask (see 1.3.3) and the vertical distance between the receiver and the water surface (Karegar et al., 2022).

1.3.2   Least Squares Inversion method

The Least Squares Inversion method is based on the idea that a reflector heights time series modeled by a B-spline curve can be derived by using the least squares approach to estimate the function nodes, along with other model parameters, by minimizing the residuals between δSNR_{model}, model oscillating part of the SNR, and the observed δSNR.

Alike the Spectral Analysis method, the units of the SNR observed by the GNSS receiver have to be converted from $dB - Hz$ to a linear scale of units by Equation 1.5, and the trend has to be removed to obtain δSNR, the oscillating part of the signal.

The function that describes δSNR is an extension of Equation 1.7. But unlike the Spectral Analysis method, where the amplitude A is considered independent to the elevation angle ϵ, the reflected power P_r is given by (Nievinski & Larson, 2014)

$$P_r = P_d |X|^2 S^2 \tag{1.10}$$

where P_d is the power incidence of the direct signal, X is a complex vector of coupled surface/antenna coefficients. In this implementation is not explicitly modeled, and $X = 1$ is assumed, and S is a coherence power attenuation factor caused by the scattering of a signal on a rough surface (Beckmann & Spizzichino, 1987), expressed as

$$S = \exp[-k^2 s^2 \sin^2(\epsilon)] \tag{1.11}$$

where k is the wavenumber given by $2\pi/\lambda$, with λ as the carrier wavelength of the signal, ϵ is the satellite elevation angle, and s is a factor that accounts for the roughness of the reflective surface. Thus, by inserting Equations 1.10 and 1.11 into 1.7, the δSNR can be written as

$$\delta SNR = A_i \cos\left(\frac{4\pi h(t)}{\lambda_i} \sin(\epsilon) + \varphi\right) e^{-k_i^2 \Lambda \sin^2(\epsilon)} \tag{1.12}$$

now with the maximum amplitude $A = 2P_d$. The factor Λ is the damping coefficient that depends on surface properties and antenna gain pattern. The subscript i denotes that those parameters are satellite system and transmission frequency dependent (e.g. GPS L1). For numerical stability, the Equation 1.12 is modified by a trigonometry identity of compound angles to

$$\delta SNR = \left(C_{1,i} \sin\left(\frac{4\pi h(t)}{\lambda_i} \sin(\epsilon)\right) + C_{2,i} \cos\left(\frac{4\pi h(t)}{\lambda_i} \sin(\epsilon)\right)\right) e^{-k_i^2 \Lambda \sin^2(\epsilon)} \tag{1.13}$$

where C_1 and C_2 are related to A and φ in such a way that

$$A = \sqrt{C_1^2 + C_2^2} \tag{1.14}$$

$$\varphi = \tan^{-1}\left(\frac{C_2}{C_1}\right) \tag{1.15}$$

To model δSNR with Equation 1.12 it is necessary to assume that the amplitudes C_1 and C_2, and the damping coefficient Λ as constants during the period of the data used for the height retrieval. On the other hand, h is considered time-varying and it is modeled by a

degree r B-spline curve to approximate the water surface height using a finite set of N nodes $h_0, ..., h_n$ as

$$h(t) = \sum_{j=1}^{n} h_j N_j{}^r(t) \tag{1.16}$$

$$N_j{}^0(t) = \begin{cases} 1 & \text{if } t_j \leq t < t_{j+1} \\ 0 & \text{otherwise} \end{cases}$$

$$N_j{}^r(t) = \frac{t - t_j}{t_{j+r} - t_j} N_j{}^{r-1}(t) + \frac{t_{j+r+1} - t_j}{t_{j+r+1} - t_{j+1}} N_{j+1}{}^{r-1}(t)$$

As mentioned before, the least squares approach is implemented to iteratively solve the nonlinear system by minimizing the residuals between δSNR_{model}, model oscillating part of the SNR, and the observed δSNR. The unknown parameters are the B-spline nodes that defined the dynamic height, the damping factor Λ, and the amplitudes C_1 and C_2. Being the last two satellite-frequency-specific parameters. Therefore, the total number of parameters M_T is given by

$$M_T = M_N + 2M_f + 1 \tag{1.17}$$

where M_N represents the number of nodes, that depends on the desired time resolution of the B-spline, thus, in the ability of the function to model fast changes in sea surface height. M_f is the number of satellite-frequency used. Thus, two parameters that represent C_1 and C_2 have to be estimated for every satellite system and transmission frequency used. For example, if GPS L1, GPS L2, and GLONASS L1 are used, then six different parameters have to be estimated. Finally, the damping factor adds only one parameter that is shared by all reflected signals.

An initial guess of the parameters has to be defined to allow the Least–squares to iterative adjust them. The values selected as initial parameters for C_1, C_2, and Λ are not affecting very much the final solution. However, in the case of the initial guess of the heights (initial B-spline nodes), the solution is very sensitive to the water level used as an approximation of the actual values. If the difference is too large, the Least-squad does not go to find the optimal solution. This is something that can happen, for example, at sites where the tide range is very large. Therefore, to ensure the quality of the initial heights, water level estimates are previously computed using the Spectral Analysis method, and the obtained heights are then used to fit a B-spline curve, whose nodes are used as initial parameters.

1.3.3   Sensing zones definition for GNSS-IR in water level monitoring

As mentioned above, the main requirement for ground-based GNSS-IR is a GNSS receiver with clear line-of-sight to sensing zones (SSZ), also known as Fresnel zone, in the water surface from where the reflected satellite signal can be detected by the antenna. A SSZ is a footprint of the signal reflected by the surface and can be represented as areas with ellipse shape of 4 m across in the direction perpendicular to satellite azimuth and longer in the radial direction. The radial length and position of the ellipse are dependent on the height of the antenna above the water surface, the elevation angle of the satellite and the GNSS transmitter frequency (e.g. L1, L2, or L5), and its orientation depends on the geodetic azimuth of the satellite with respect to the antenna (Roesler & Larson, 2018). In practice, the signal of every visible satellite projects one sensing zone that is changing while the satellite moves along its orbit, e.g. the sensing zone becomes smaller and closer to the antenna as the elevation angle increases.
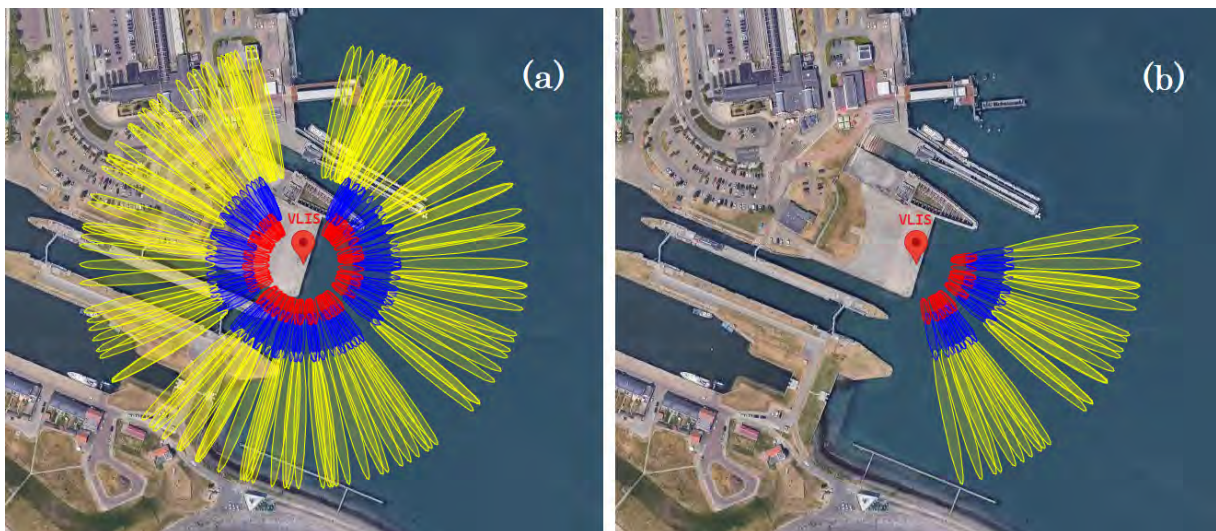

Figure 1.3.3.1: Sensing zones of the GNSS station, code name "vlis", at the Vlissingen Port, Netherlands. The reflected GPS L1 signal is projected on a Google Earth image. Ellipses represent the footprint where the colors symbolize different elevation angles: yellow ellipses correspond to 5°, blue to 10°, and red to 15°. (a) Reflection zones without azimuth mask. (b) Reflection zones corresponding to the azimuthal mask corresponding to 80°-170°. Source: https://gnss-reflections.org/rzones

As can be observed from Figure 1.3.3.1, not all the SSZ are reflections coming from the water surface. Some are covering areas partially or completely occupied by land and/or structures, generating measurements with superimposed oscillations indicating that come from multiple reflective surfaces and are not suitable to retrieve water levels (Löfgren et al., 2014). To remove these undesired measurements it is necessary to establish a

reflection mask defined by an azimuth mask and an elevation angle mask. The definition of the azimuth mask consists of omitting any azimuth in which there is an obstructed line-of-sight to the water surface. The main factors to define the limits of the mask are the shape of the body of water and the presence of obstacles around the receiver. The example of Figure 1.3.3.1 (b) shows how all the reflections from land and structures around the antenna area site were omitted. Another relevant factor when defining the azimuth mask is the latitude of the site where the receiver is located. GNSS constellations have no satellites abutting the polar regions, resulting in a region without data in the north or south direction (see 1.3.3.2), depending on the hemisphere where the antenna is located, the extent of which varies depending on the latitude. The effect of this limitation is evidenced in Figure 1.3.3.1 (b), where a permanent gap is observed to the north.
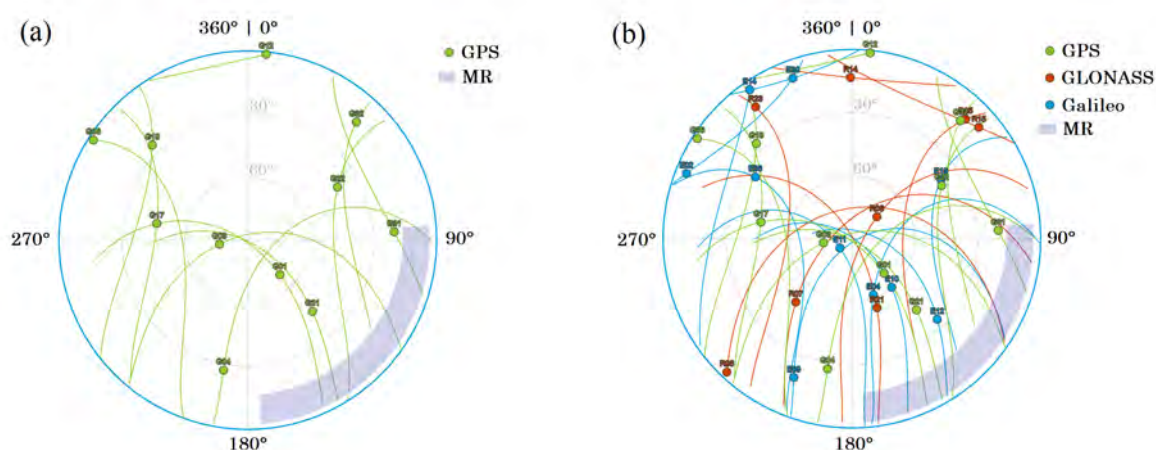

Figure 1.3.3.2: Sky plot simulation at the location of the GNSS station, code name "vlis", at the Vlissingen Port, Netherlands (2022-12-22 03:30 UTC + 00:00). (a) Only GPS satellites are observed by the receiver at a specific time. (b) GPS, GLONASS, and Galileo satellites are observed by the receiver at a specific time. In both sky plots, the blue regions called "RM" was added to represent the allowed "measurements region" based on the azimuth and elevation mask established for GNSS-IR implementations. Sky plot simulations from: `https://www.gnssplanning.com`

On the other hand, the elevation angle mask definition is less intuitive and requires an analysis of the surrounding area combined with the antenna height above the water surface (e.g. above mean sea level). An initial recommendation in choosing the elevation mask is to omit signals from satellites with elevation angles greater than 25° and less than 4°. The upper limit is based on the attenuation observed in the amplitude of the δSNR when the elevation angle increases. This can be observed in Figure 1.3.0.1 where the amplitude of the oscillations is maximum proximal to the horizon (0°) and is dampened when the satellite moves towards the nadir of the receiver, e.i. the greater the elevation angle, the smaller the oscillations in the signal, and previous studies shown that measurements

from angles greater than 25° have a bigger uncertainty (Purnell et al., 2020), making them less meaningful for water level retrieval. At the same time, high elevation angles in combination with a small height of the antenna above the water surface cause the reflections to occur very close to the antenna, e.g. the position of a sensing zone from 25° with an antenna height of 9 m above the water will happen approximately 10 m away, thus especial care is needed to examine if signals could be affected by obstacles in the vicinity.

In the case of the lower limit, the direct signal observed at angles less than 4 degrees is more affected by tropospheric delay than that from satellites orbiting higher above the horizon, since the signal has to travel a longer path through the lower atmosphere (Purnell et al., 2020).

In principle, the existence of a reflection area on the water surface is the essential requirement for the implementation of GNSS-IR to recover water levels. However, for real-time monitoring, the importance of SSZ goes further because the extent of the reflection area largely defines the number of SNR observations available for the calculation of the water level at each instant of time. When a mask is imposed (azimuth and/or elevation angle), it means that all measurements observed by the receiver coming from angles outside the set mask range must be ignored. If the reflection area is too short, there is a possibility that at some time all available measurements will be discarded, creating a data lack in the observation. An example of this is shown in Figure 1.3.3.2, where it can be noticed, that the angular mask, highlighted in blue, is very reduced, causing no satellite observations to be available at the time of the simulation, (2022-12-22 03:30 UTC + 00:00).

As can be deduced by comparing Figure 1.3.3.2 (a) and (b), the capability of the antenna to receive signals of various GNSS constellations and multiple frequencies is another factor that limits the number of measurements available at every time. In Figure 1.3.3.2 (a), only 11 GPS satellites are detected by the receiver while in (b) 29 satellites from several constellations can be measured, showing that having observations from more than one constellation increases the number of available signal sources, helping to deal with the data lack caused by small reflections area since the receiver gets signals from more satellites. Nevertheless, the distribution of the satellites is not homogeneous and varies from time to time. As a result, when the reflection area is small as in the example of 1.3.3.2, receiving signals from several satellite constellations is not a guarantee to avoid data lack. This is particularly relevant when monitoring the level in real-time because the possibility of knowing the immediate state of the water level is limited to the availability of measurements at that instant in time. If the conditions of a very restricted reflection area and access to a reduced number of constellations and frequencies, the amount of data

may decrease to the point that a real-time implementation is not possible.

The challenge of sea-level sensing The definition of the reflection mask for implementing GNSS-IR to sea level monitoring follows, in general, the procedure that was previously described by using the coastline as the main reference to first, define the azimuth mask, and second, choose the higher elevation angles to be used. The latter is especially relevant since most GNSS stations installed near the coastline are located close to civilian structures, such as ports and marinas, where the presence of docks or other harbor structures should be taken into account to avoid that the SSZ that are closer to the receiver stat including the shore or structures in the vicinity. An example of this is shown in Figure 1.3.3.1, where most of the reflections coming from the northeast quadrant should be omitted due to the presence of harbor structures. Additionally, it is important to study the existence of passing routes of vessels such as small boats or large ships, especially in the vicinity of docks. Temporal obstacles in a SSZ can alter the signals measured by the receiver, and subsequently, decrease the accuracy of the retrieved heights Karegar & Kusche (2020).

In the case of real-time sea level monitoring with GNSS-IR, the capacity to track the sea level changes strongly depends on the possibility of constantly receiving observations reflected from the sea surface. The existence of data lack caused by a very limited reflection area implies a time during which it is not possible to estimate the sea level, and consequently, to guarantee the uninterrupted operation of the processes for which having this information is essential. In the case of cyclical sea level changes such as ocean tides, the sea level could be modeled based on previous height retrievals made by with the GNSS-IR implementation (e.g. water level time series) or ocean tides model, in order to estimate sea level during this period with lack of measurements. However, in the presence of sudden level changes like storm surges or tsunamis, the existence of data lack is critical, as any previous data or models can be used to estimate the influence of these changes.

The challenge of river water-level sensing In the implementation of GNSS-IR in rivers the definition of the reflection area is limited, by the shape and extension of the water surface of the river. But, unlike sea level monitoring where only the coastline defines the limit between water and land, rives have a limited width, adding an additional constraint, especially when setting the lower limit of the elevation angle mask because the corresponding SSZ may reflect off the opposite bank of the river. And the definition of the river boundaries becomes more challenging when it is taken into account that the boundaries of the river can vary throughout the different times of the year. For instance,

areas that are covered by water when the river level is high, due to rain or snow melt, may be uncovered when the river level falls. Likewise, the presence of in-water structures such as dikes, jetties, or piers should be considered and omitted by means of the mask. The same applies to the presence of structures in the vicinity, such as bridges, which may interfere with the measured signals in the direction in which they are located.

In addition, the wide rivers that may be subject to the implementation of GNSS-IR are commonly used for navigation and commerce, causing boats, river cruisers, and large transport vessels to be constantly in transit. The presence of these shipping lanes must be studied to prevent them from causing interference in the data used to estimate river level.

1.4   Contribution of this study

As previously mentioned, real-time water level monitoring is essential for water resources management, environmental protection, hazard prevention, and early warning of flood risk. Therefore, the aim of this thesis is to evaluate real-time water level measurements through an implementation of a Kalman Filter and a technique called GNSS-IR. It is of great interest to test the real-time implementation in sea-level and river-level monitoring and its capacity to detect sudden level changes caused by extreme events. For this, real-time water levels retrieved by implementing an Ensemble Kalman Filter (EnKF) are going to be investigated in several scenarios: (i) real-time sea level monitoring, (ii) real-time coastal storm surges detection, (iii) real-time river level monitoring, (iv) real-time river flash floods detection, and finally, (v) low-cost antennas data will be explored for the evaluation of real-time river level determination.

A real-time approach must take into consideration efficient time for data processing, but also the time required for data measurement and possible latency due to data transfer (when data processing is not in situ). For this reason, the use of the SNR with observation rates of one measurement every 15 and/or 30 seconds will be assessed. Daily files of $SNR-ready$ data will be used to simulate real-time δSNR observations with the aforementioned sample rates and the resulting water levels will be compared to co-located tide or river gauge level series, whose water levels are assumed to be ground-truth values.

1.5 Thesis structure

This thesis is composed of 5 chapters. Chapter 1 corresponds to the introduction where the importance of real-time water level monitoring is described, as well as the contributions of the GNSS Interferometric-reflectometry (GNSS-IR) as an alternative for water surface height determination, as well as the principle of GNSS-IR technique and related methods, are mentioned. Section 2 overlooks the current state of the Kalman filter (KF) approach for GNSS-IR and details the approach for water-level retrieval evaluated in this thesis. Moreover, in Chapter 3, the Study area, data collection, and software are explained. Chapter 4 presents the results and narrates the discussion. Lastly, Chapter 5 corresponds to the conclusion and recommendations.

Chapter 2

Water level determination using a Kalman filter approach in real-time

The Kalman filter (KF) is an algorithm that uses a series of noisy and occasionally inaccurate measurements to update the linear projection of a system of variables on the set of available information over time. The basic idea of the filter is to sequentially predict and update the state of a system (Kalman, 1960), hereinafter state vector x, and its corresponding uncertainty, the covariance matrix P, by first using the best guess of the system's previous state $\hat{x}_{t-1|t-1}$ and a linear model F_t that explains the time evolution of the system to estimate the future state by

$$\hat{x}_{t|t-1} = F_t \hat{x}_{t-1|t-1} + w_t \tag{2.1}$$

$$\hat{P}_{t|t-1} = F_t \hat{P}_{t-1|t-1} F_t^T + Q_t \tag{2.2}$$

where $\hat{x}_{t|t-1}$ and $\hat{P}_{t|t-1}$ are the predicted state and covariance respectively, w_t is the zero mean multivariante normal distribution $w \sim \mathcal{N}(0, Q)$, with Q_t as the system noise covariance matrix.

Then, at the moment new measurements z_t are observed, the predicted state and its covariance are updated with a linear measurement model H_t that explains the relationship between the state and the measurements by

$$\hat{x}_{t|t} = \hat{x}_{t|t-1} + K_t \tilde{y}_t \tag{2.3}$$

$$\hat{P}_{t|t} = (I - K_t H_t) \hat{P}_{t|t-1} \tag{2.4}$$

where I is an identity matrix, $\tilde{y}_t$ are residuals defined by

$$\tilde{y}_t = z_t - H_t \hat{x}_{t|t-1} \tag{2.5}$$

with $H_t \hat{x}_{t|t-1}$ as modeled measurements based on the predicted state. The Kalman gain K_t minimizes the residual error, and is defined by

$$K_t = \hat{P}_{t|t-1} H_t^T S^{-1} \tag{2.6}$$

where S is the innovation covariance matrix defined by

$$S_t = H_t \hat{P}_{t|t-1} H_t^T + R_t \tag{2.7}$$

with R_t as the measurements noise covariance matrix.

This property of updating the system's state based on data collected over time enables the KF to generate computationally effective real-time solutions. However, the assumption that both the observation and measurement models are linear restricts the application of this filter to real-life implementations. As a result, alternative methods for dealing with nonlinear systems, such as the Extended Kalman filter (EKF) (Crassidis & Junkins, 2011), have been developed. This technique follows the same prediction and update scheme of the conventional KF. The difference is that the observation and measurement models are nonlinear, denoted by $f(x)$ and $h(x)$ respectively so that Equations 2.1 and 2.5 are rewritten as

$$\hat{x}_{t|t-1} = f(\hat{x}_{t-1|t-1}) + w_t \tag{2.8}$$

$$\tilde{y}_t = z_t - h(\hat{x}_{t|t-1}) \tag{2.9}$$

Hence, the nonlinear models are linearized by computing the Jacobians, causing F and H to take the form

$$F_t = \frac{\delta f}{\delta x}\Big|_{\hat{x}_{t-1|t-1}} \qquad\qquad H_t = \frac{\delta h}{\delta x}\Big|_{\hat{x}_{t|t-1}}$$

This approach has been widely used in several applications such as positioning and navigation with GNSS. However, it is prone to divergence when the system is highly nonlinear (Ljung, 1979), as, for instance, Equation 1.12 that can be considered the measurement model in GNSS-IR inversion method. For this reason, alternative approaches of the KF have to asses for real-time water level retrieval.

2.1 Current state of Kalman filter approach for GNSS-IR

The retrieval of water level heights using GNSS-IR methodologies has been extensively studied in recent years, and the exploration of different techniques to optimize the water surface estimation, the accuracy of the retrieved heights, and improve its temporal resolution has included the use of various KF approaches. In the study of Santamaría-Gómez et al. (2014) a KF was employed to isolate the SNR data dominated by sea-surface reflections so that the sea surface height could be used to link the height of the GPS antenna with the zero reference of a tide gauge considered the need for other leveling instruments. Afterward, Santamaría-Gómez & Watson (2016) proposed the optimization of the unknown receiver bandwidth and the estimation of frequency changes in the SNR oscillation through an EKF/smoother algorithm and other corrections to improve the SNR interference near the horizon.

The monitoring of coastal hazards has also been done using the KF method. In the Kim et al. (2021) study, the use of multi-band GNSS signals, choosing the best processing window and utilizing Kalman filtering for height rate determination allowed the GNSS-IR approach to be improved in the post-event analysis to detect extreme changes in water level (e.i. tsunamis and storm surges).

Focusing on the use of Kalman filters for real-time water level retrieval, which is the main objective of this thesis, we came across the implementation shown by Strandberg et al. (2019) for real-time sea level monitoring, in which the use of Unscented Kalman filter (UKF), which is based on the unscented transform (Julier & Uhlmann, 1997), was explored as an alternative to deal with highly nonlinear measurement models.

The unscented transform is a deterministic sampling method to estimate the first moments of a random variable by propagating a minimal set of sample points, called sigma points, through a transformation (e.g. nonlinear measurement model), determining the posterior mean and covariance for any nonlinearity (Wan & van der Merwe, 2001), avoiding the linearization of the system (e.i. no explicit computation of Jacobians).

The definition of dynamic height sea level and the state vector (unknown parameters) in this approach is similar to the one used in the least-squares inversion method described in Section 1.3.2. However, due to the nature of the real-time processing, the number of scaling coefficients in the state vector is limited. Therefore, a dynamic update of the state vector was implemented by establishing a time window for a given interval bounded by the

scaling coefficients. Once the time of the last measurement reaches the maximum limit, the scaling coefficients contained in the state vector are updated by removing the oldest coefficient, shifting one space to the position of the remaining ones, and adding a new one that determines the new limit of the time interval. This allows the number of state vector elements to be time-invariant. In the case of the covariance matrix, it is also updated by shifting the values in the matrix and adding a new variance for the newest coefficient. A more detailed explanation can be also found in Strandberg (2020). The results of this study showed that sea level real-time monitoring with GNSS-IR is possible using the UKF and a dynamic B-spline approach, obtaining water level retrievals in near-real-time on a similar level of precision as the least-squares inversion in post-processing.

2.2 Kalman filter approach for water-level retrieval

The findings of Strandberg et al. (2019) showed that sea level real-time monitoring with GNSS-IR is possible using the UKF and a dynamic B-spline, obtaining water level retrievals with good precision. Nonetheless, the goal of this thesis is to implement a Kalman filter approach for real-time water level retrieval not only for sea surface level but also for inland water which tends to have a constant level over time, and whose variations respond mainly to atmospheric events. The imposition of a B-spline dynamic model in this kind of surface can cause the appearance of artifact variations in the water level when the spacing between nodes is not optimal. If the spacing is too small, the occurrence of artificial variations may increase. On the other hand, if the spacing is too large, it decreases the ability of the model to represent variations that may occur over short periods, such as a sudden rise caused by strong rainfall.

Additionally, the UKF has proven to be an easily implemented tool in multiple applications. However, this filter requires the prior setting of several tuning parameters (Wan & van der Merwe, 2001) that vary the way the filter generates the results. In the same way, the filter can be unstable depending on the values of system noise and measurement noise that are chosen affecting the updating of the covariance matrix, easily causing it to be negative definite, which is not compatible with the unscented transform method used in UKF. For this reason, the Ensemble Kalman filter (EnKF) as presented by Crassidis & Junkins (2011) is going to be explored in this thesis as an alternative approach for highly nonlinear models that can be implemented for real-time water retrieval.

The EnKF is a prominent approach in various geoscientific disciplines since it is a Monte Carlo-based version of the KF for very large-dimensional, nonlinear, and non-Gaussian

state estimation problems. The method is based on the idea that the sample covariance can be used to replace the covariance matrix P in of the KF by employing a collection of N state vectors (also called ensembles). Avoiding numerical issues that can occur in trying to maintain and use the state covariance matrix in other KF implementations (Crassidis & Junkins, 2011). The samples collection x_t^j with $j = 1, ..., N$ is defined only at the beginning of the implementation and is defined based on an initial state vector x_0 and an initial covariance P_0 as

$$\hat{x}_t^j = \mathcal{N}(x_0, P_0) \tag{2.10}$$

As any other KF, the recursive procedure is separated into a prediction step and an update step. The prediction step consists of passing the sample collection through a model to estimate multiple future states of the system. The method can be implemented with a nonlinear system model f so that by

$$\hat{x}_{t|t-1}^j = f(\hat{x}_{t-1|t-1}^j) + w_t^j \tag{2.11}$$

where w_t is the zero mean multivariante normal distribution $w \sim \mathcal{N}(0, Q)$, with Q_t as the system noise covariance matrix. The subscript $(t|t-1)$ and $(t-1|t-1)$ denote the predicted and prior states respectively.

The update step occurs at the moment new observations are available, and consists of the use of the Kalman gain K and innovation residuals $\tilde{y}_t^j$ to update the predicted collection of samples by

$$\hat{x}_{t|t}^j = \hat{x}_{t|t-1}^j + K_t \tilde{y}_t^j \tag{2.12}$$

where subscript $(t|t)$ denotes that the updated stated corresponds to the current time. The Kalman gain K is computed using

$$K_t = P_t^{xy}(P_t^{yy})^{-1} \tag{2.13}$$

where P_t^{yy} is an approximation of the cross-covariance of the modeled observations given by

$$P_t^{yy} = \frac{1}{N-1} \sum_{j=1}^{N} [\hat{y}_t^j - \hat{y}_t][\hat{y}_t^j - \hat{y}_t]^T + R \tag{2.14}$$

where $\hat{y}_t$ is the mean of a collection of modeled measurements defined with the predicted states $\hat{x}_{t|t-1}^j$ and the nonlinear measurement model h and given by

$$\hat{y}_t^j = h(\hat{x}_{t|t-1}^j) + v_t \tag{2.15}$$

with v_t as the zero mean multivariante normal distribution $v \sim \mathcal{N}(0, R)$, with R_t as the

measurements noise covariance matrix. And P_t^{xy} given by

$$P_t^{xy} = \frac{1}{N-1} \sum_{j=1}^{N} [\hat{x}_{t|t-1}^j - \hat{x}_{t|t-1}][\hat{y}_t^j - \hat{y}_t]^T \tag{2.16}$$

where $\hat{x}_{t|t-1}$ is the mean of the collection of predicted states.

After the update step, the resulting updated state vector $\hat{x}_{t|t}$ is computed as the mean of the states obtained with Equation 2.12.

The covariance matrix P_t is not needed in the computation of the EnKF. However, it can be approximated using the sample covariance through

$$\hat{P}_t = \frac{1}{N-1} \sum_{j=1}^{N} [\hat{x}_{t|t}^j - \hat{x}_{t|t}][\hat{x}_{t|t}^j - \hat{x}_{t|t}]^T \tag{2.17}$$

2.3 Implementation for real-time water-level retrieval

In this study, the EnKF will be used to estimate in real-time the height of a water surface with respect to a GNSS antenna by using the oscillating part of the observed SNR as measurements and the nonlinear measurement model described by Equation 1.12. To operate the filter in real time, the SNR must be detrended in real time as well. The trend part of a satellite arc mostly depends on the antenna gain pattern and the strength of the satellite signal, and then it is typically constant. Thus, one way to remove it in real time is by utilizing the average of a few of the most recent passes of the same satellite to approximate the trend.

The elements of the system state vector in the EnKF implementation are n normalized weighting factors W used in the prediction step and the components of the Equation 1.12, the surface height h, the damping factor Λ, amplitude A, and phase delay φ. The last two parameters are satellite-frequency-specific. Hence, two state vector elements have to be estimated for every satellite system and transmission frequency used. The height and the damping factor are shared by all reflected signals, so each adds only one element to the state vector. The total number of state vector elements M is given by

$$M = n + 2M_f + 2 \tag{2.18}$$

where M_f is the number of satellite-frequency used. For example, if GPS L1, GPS L2,

GLONASS L1, and GLONASS L2 are used, then $M_f = 4$.

The initial state vector x_0 elements can be defined with the δSNR from 24 hours previous to the instant of time in which the filter will be started. The initial height h is estimated by using the LSP method to obtain an approximation of the current water level. This approximation should be estimated with the data closest to the time the filter will start. Otherwise, it is not possible to guarantee that the initial height estimate is similar to the actual water level, making it difficult for the EnKF to converge. This is especially relevant when monitoring sea level, which is expected the water height to be constantly varying due to tidal influence. The initial amplitude A can be estimated as the value of 3σ of the δSNR, and the phase delay φ can be initialized as zero. Finally, good guesses of the damping factor Λ were empirically defined as 0.1 for filter implementations in sea level monitoring and 0.01 for river level monitoring.

The initial covariance matrix P_0 needed to define the sample collection of the EnKF with Equation 2.10 is defined with the values shown in Table 2.1. The values were defined as high variances so that the sample spreads out around the initial values and allows the filter to converge towards the best estimates of the state of the system. The weighting factors W are initialized with 0 variance.

Table 2.1: Initial covariance matrix P_0 values (diagonal values) used when starting the EnKF.

Parameter	Variance
h	$1x10^{-2}m^2$
A	$1x10^{-2}(V/V)^2$
φ	$1x10^{-2}rad^2$
Λ	$1x10^{-5}$

Once the filter is started, the prediction step is defined to

$$\hat{x}_{t|t-1} = \hat{x}_{t-1|t-1} + \sum_{i=1}^{n} W_i \Delta h_{t-i} + w_t \tag{2.19}$$

where the best prediction of the future state $\hat{x}_{t|t-1}$ is the previous state $\hat{x}_{t-t|t-1}$ plus a weighted moving average of the height changes δh_{t-i} determined in n^{th} previous times, multiply by the weighting factors W_i, plus the process noise w_t that accounts for the possible error in the prediction step.

At the beginning of the implementation, the weighting factors are estimated as

$$W_i = \frac{1}{\Delta t^i}$$

where Δt is the sample rate of the SNR used in the implementation. And normalized so that $\sum_{i=1}^{n} W_i = 1$.

Subsequently, the nth power factors are added to the state vector so that the filter takes care of updating them based on the evolution of the data.

Under normal conditions, no significant changes are expected in water level in short periods of time (e.g. few millimeters even in coastal areas with large tidally influenced variation). Likewise, as was explained by Strandberg et al. (2016), the other state elements can be considered to be slowly variable even in long periods of time (e.g. days) and affected in part by surface conditions that are difficult to predict. For instance, the amplitude is mainly influenced by satellite signal strength, receiver characteristics, and electromagnetic properties of the reflecting surface while the phase delay is derived from the same electromagnetic properties (Nievinski & Larson, 2013). Therefore, in this implementation, all these external factors are considered constant and their changes as random processes defined by small process noises, allowing the elements of the state vector to change during the update process if the residuals are improved.

The selected values for the process noises determine how well the EnKF implementation will be able to estimate the water level and the other parameters of the system state. Inadequate values can prevent the filter from adapting to environmental changes, making it unable to provide good estimates. For example, if the height process noise is small, the filter will not be able to modify the height following the level variations caused by tides or derived by weather conditions. On the other hand, if the process noise is too large, the filter could estimate sudden changes in the water level that should be absorbed by the other parameters. As the real water level dynamic is site-specific and also depends on external factors, the right process noise is difficult to be defined. In this study, the process noise for every tested site was established to guarantee a stable solution under the site conditions at the moment the data was measured. The same process noise was defined for all amplitude and phase delay parameters. In the case of the weighting parameters, a small system noise of $1x10^{-11}$ is added to allow the filter to add small updates to the factors.

In the update step, as the real measurement noise is unknown, is defined as the variance of the δSNR.

The simulated real-time solution performance is evaluated by comparing the results along with tide or river gauges time series by using Root-Mean-Square Error (RMSE), which is a common way to estimate how predicted values match up to observed values by

$$RMSE = \sqrt{\frac{\sum_{j=1}^{N} \left(X_{pred_j} - X_{obs_j}\right)^2}{N}} \tag{2.20}$$

where X_{pred} and X_{obs} are vectors of N the predicted and observed values respectively.

Chapter 3

Study area and data collection

This chapter details the selected sites where the real-time implementation is performed and the instruments used for data measurement, as well as the GNSS and the co-located tide/river gauges data set used. It also gives a close-up of the data sets and *gnssrefl* software used in the data collection process.

3.1 Study areas

In order to assess the precision of the Kalman filter-based retrievals, we used SNR data from five test sites with different characteristics. Two of them on the coast and three on riverbanks. All the GNSS antennas are co-located to tide or river gauge stations, whose water level records were used in the validation process as a reference and are assumed to provide ground-truth values.

3.1.1 TGMX site

TGMX test installation is a site located at Puerto Morelos, Quintana Ro, Mexico, and consists of a GNSS antenna co-located with a Radar tide gauge. See Figure 3.1.1.1. Location data of the site is detailed in Table 3.1. The GNSS station is administrated by the University NAVSTAR Consortium (UNAVCO) and the National Autonomous University of Mexico (Spanish: Universidad Nacional Autónoma de México, UNAM) and consists of a Trimble TRM59800.00 choke ring antenna paired with a Trimble NETR9

receiver recording GPS, GLONASS, and Galileo data at a rate of 15 Hz. Rinex data can be obtained from the UNAVCO data center (`https://www.unavco.org/data/gps-gnss/gps-gnss.html`) using the 4 characters name "tgmx".
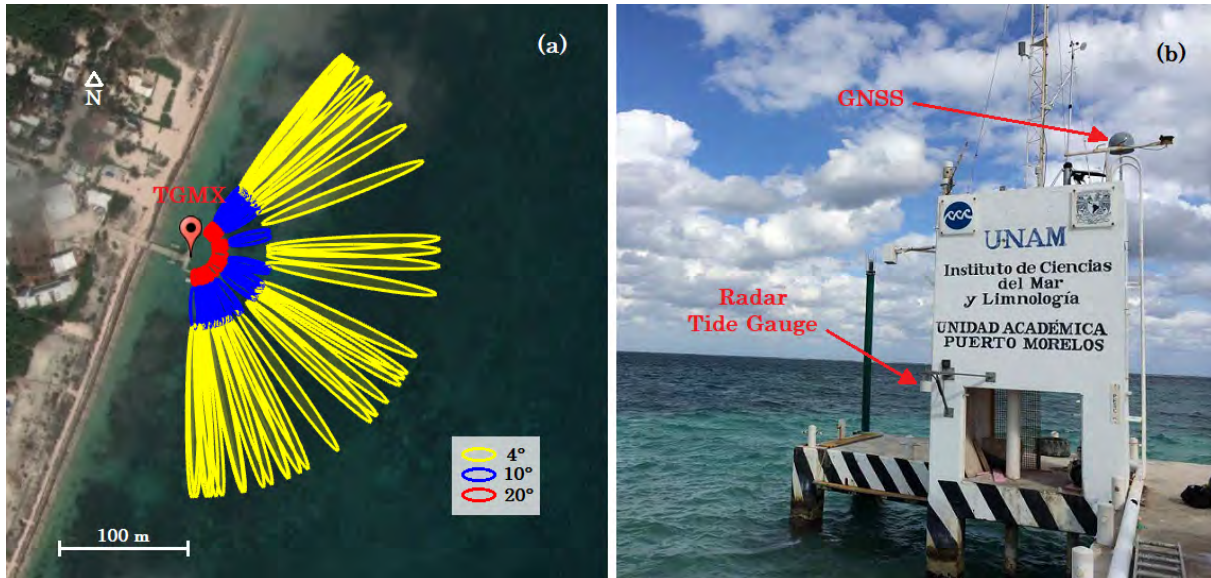
Figure 3.1.1.1: Test site TGMX. (a) Location of the GNSS antenna and tide gauge in Puerto Morelos, Quintana Ro, Mexico. Footprints of the reflected GPS signals are projected on a Google Earth image. Reflection zones corresponding to azimuth 30°–190° and elevation 4° and 20°. (b) The GNSS antenna was installed on top of a fixed structure in a dock. The tide gauge is also attached to the same structure. Source: `https://gnss-reflections.org/rzones`

Table 3.1: Approximated geographical information of the station TGMX. Source: `https://gnss-reflections.org/rzones`

Station	TGMX
Latitude	20.86811584
Longitude	-86.86685458
Ellipsoidal Height (m)	-4.665
Reflection Height (m)	7.185

The tide gauge is administrated by United Nations Educational, Scientific and Cultural Organization (UNESCO) and consists of a RADAR gauge that records water-level data at a rate of 1 minute in units of mm with an approximated accuracy of 1 cm. Sea level records can be obtained from the UNESCO data center (`http://www.ioc-sealevelmonitoring.org/`) using the station code "pumo2".

The reflection area of this site was mainly defined on the coastline, this can be observed in Figure 3.1.1.1 (a). Elevation angles larger than 20° were omitted due to those can introduce reflections from the dock.

3.1.2 CALC site

CALC test installation is a site located in Calcasieu Pass, Louisiana, United States, and consists of co-located GNSS antenna and an Acoustic-sensor tide gauge. See Figure 3.1.2.1. Location data of the site is detailed in Table 3.2. The GNSS antenna is administrated by National Oceanic and Atmospheric Administration (NOAA) and the National Geodetic Survey (NGS) and consists of a Trimble TRM115000.00 antenna (Trimble Zephyr 3 Geodetic Antenna) paired with a Trimble ALLOY receiver recording GPS, GLONASS, and Galileo data at a rate of 15 Hz. Rinex data can be obtained from the NOAA data center (`https://geodesy.noaa.gov/CORS/data.shtml`) using the 4-characters name "calc".
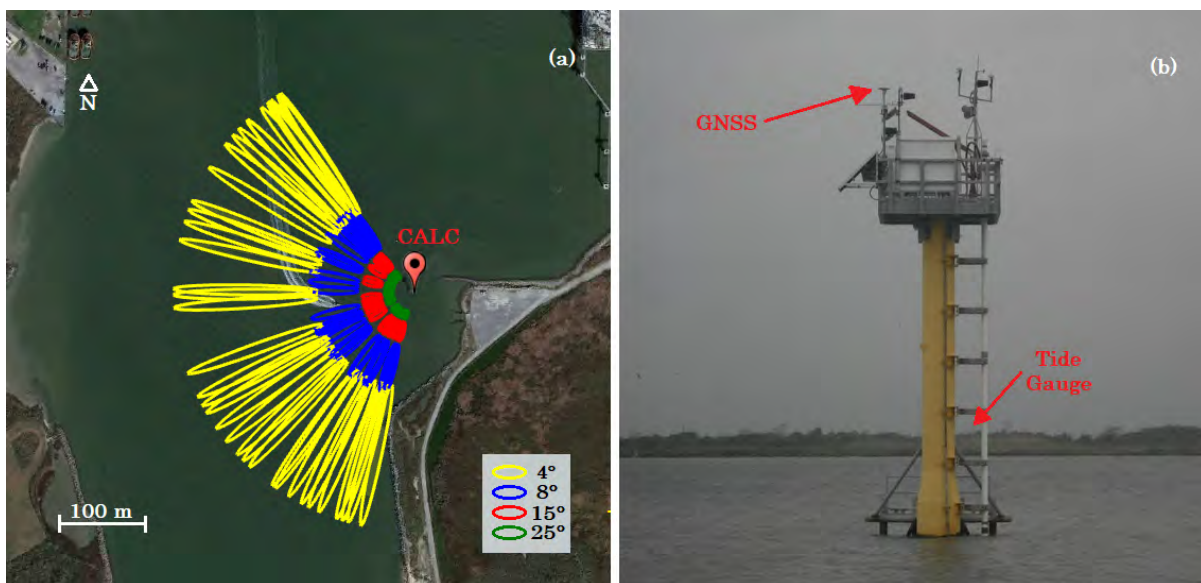
Figure 3.1.2.1: Test site CALC. (a) Location of the GNSS antenna and tide gauge in Calcasieu Pass, Louisiana, United States. Footprints of the reflected GPS signals are projected on a Google Earth image. Reflection zones corresponding to azimuth 190°–340° and elevation 4° and 25°. (b) The GNSS antenna was installed on top of a fixed structure in a dock. The tide gauge is also attached to the same structure. Source: `https://gnss-reflections.org/rzones`

The tide gauge is administrated by NOAA in the National Centers for Environmental Information (NCEI) and consists of an acoustic-sensor gauge that records water-level data at a rate of 6 minutes in units of mm with an approximated accuracy of 1 cm. Sea level records can be obtained from the NCEI data center (`https://www.ngdc.noaa.gov/hazard/tide/#`) using the 7-digit National Ocean Service (NOS) station ID: 8768094.

As shown in Figure 3.1.2.1 (b), both instruments are housed in a structure specifically built to resist hurricanes and other significant storms. When severe disasters occur, the strengthened stations are better equipped to continue operating and provide crucial in-

formation on water levels and winds that help emergency response agencies.

Table 3.2: Approximated geographical information of the station calc. Source: `https://gnss -reflections.org/rzones`

Station	CALC
Latitude	29.76813859
Longitude	-93.34288999
Ellipsoidal Height (m)	-15.180
Reflection Height (m)	12.460

The reflection area of this site was mainly defined on the coastline, this can be observed in Figure 3.1.2.1 (a). Elevation angles larger than 25° were omitted due to those can introduce reflections from the basement structure.

3.1.3   GWES site

GWES test installation is a site located in Wesel, Germany. This station is administrated by the German Federal Institute of Hydrology (German: Bundesanstalt für Gewässerkunde, BfG). It consists of co-located GNSS antenna and a pressure-sensor river gauge. See Figure 3.1.3.1. Location data of the site is detailed in Table 3.3 The equipment consists of a Leica AR25 (LEIAR25.R3 with Radome LEIT) antenna paired with a LEICA GR10 receiver recording GPS, GLONASS, and Galileo data at a rate of 30 Hz. Rinex data can be obtained from the (BfG)(`https://www.bafg.de/DE/05_Wissen/ 02_Veranst/2021/2021_11_23_schmitz.html`). The station 4-characters name is "gwes".

The river gauge consists of a pressure-sensor gauge that records river-level data at a rate of 15 minutes in units of *cm* with an approximated accuracy of 3 *cm*. River level records from the last thirty days can be obtained from the German Federal Waterways and Shipping Administration (WSV) (`https://www.pegelonline.wsv.de/gast/start`) using the station name "wesel".

Figure 3.1.3.1: Test site GWES and WESL. (a) Location of the GNSS antenna GWES, the PRP WESL, and tide gauge in Rhine river, Wesel, Germany. Footprints of the reflected GPS signals are projected on a Google Earth image. Reflection zones corresponding to azimuth 260°–320° and elevation 5° and 15°. (b) Both antennas were installed on top of a stilling well river structure. The tide gauge is in the same structure. Source: `https://gnss-reflections.org/rzones`

Table 3.3: Approximated geographical information of the station GWES. Source: `https://gnss-reflections.org/rzones`

Station	gwes
Latitude	51.64614917
Longitude	6.60678307
Ellipsoidal Height (m)	73.057
Reflection Height (m)	16.500

As shown in Figure 3.1.3.1 (b), both instruments are housed in a structure built on the river bank. The reflection area of this site was mainly defined on the river banks, this can be observed in Figure 3.1.3.1 (a). Elevation angles less than 5° were omitted due to their approach to the opposite river bank. All the reflections from the southwest were ignored because they may be affected by interference due to the presence of the bridge.

3.1.4   WESL site

WESL test installation was temporally placed from March 2020 to November 2021 in Wesel, Germany (Karegar et al., 2022). The location of this site corresponds to the same

GWES site, co-located with a pressure-sensor river gauge administrated by the German Federal Institute of Hydrology (German: Bundesanstalt für Gewässerkunde, BfG). See Figure 3.1.3.1. Location data of the site is detailed in Table 3.4. The equipment consists of a Raspberry Pi Reflector (PRP). It includes a low-cost single-frequency (L1) GPS module and a GPS navigation antenna connected to a Raspberry Pi computer and a cellular modem. The receiver is recording GPS L1 data at a rate of 1 Hz. Processed data can be obtained from `https://doi.org/10.1029/2021wr031713`.

The river gauge is a pressure-sensor that records river-level data at a rate of 15 minutes in units of *cm* with an approximated accuracy of 3 *cm*. River level records from the last thirty days can be obtained from the German Federal Waterways and Shipping Administration (WSV) (`https://www.pegelonline.wsv.de/gast/start`) using the station name "wesel".

Table 3.4: Approximated geographical information of the station WESL.

Station	WESL
Latitude	51.64614917
Longitude	6.60678307
Ellipsoidal Height (m)	73.057
Reflection Height (m)	13.000

As shown in Figure 3.1.3.1 (b), the reflection area defined is the same as the one established for the GWES site.

3.1.5 BEUE site

BEUE test installation is temporally placed since March 2020 until today in the Rhine river in Bonn-Beuel, Germany. See Figure 3.1.5.1. A pressure-sensor river gauge administrated by the German Federal Institute of Hydrology (German: Bundesanstalt für Gewässerkunde, BfG) is located in the vicinity. Location data of the site is detailed in Table 3.5. The equipment consists of a Raspberry Pi Reflector (RPR). It includes a low-cost single-frequency (L1) GPS module and a GPS navigation antenna connected to a Raspberry Pi computer and a cellular modem. The receiver is recording GPS L1 data at a rate of 1 Hz.

The river gauge consists of a pressure-sensor gauge that records river-level data at a rate of 15 minutes in units of *cm* with an approximated accuracy of 3 *cm*. River level

records from the last thirty days can be obtained from the German Federal Waterways and Shipping Administration (WSV) (`https://www.pegelonline.wsv.de/gast/start`) using the station name "bonn".

Table 3.5: Approximated geographical information of the station BEUE.

Station	BEUE
Latitude	50.728231
Longitude	7.118579
Ellipsoidal Height (m)	-
Reflection Height (m)	4.500

As shown in Figure 3.1.5.1 (b), the instrument is placed in a steel rod attached to a pier on the river bank. The reflection area of this site was mainly defined on the river banks, this can be observed in Figure 3.1.5.1 (a). Elevation angles less than 3° were omitted. Most of the northwest reflections were ignored because they may be affected by the interference of the pier.

Figure 3.1.5.1: Test site BEUE. (a) Location of the PRP GPS antenna in Rhine river, Bonn-Beuel, Germany. Footprints of the reflected GPS signals are projected on a Google Earth image. Reflection zones corresponding to azimuth 140°–280° and elevation 3° and 20°. (b) The PRP was installed on a pier. Source: `https://gnss-reflections.org/rzones`

3.2   *gnssrefl* **software Overview**

In this thesis, the real-time implementation is going to be performed as an extension of the *gnssrefl* open-source python software package (Larson, 2021). This software was created primarily for ground-based GNSS-IR applications, and it can currently estimate reflector heights using spectral or inversion methods, although it is limited to non-real-time applications. Manual and installation guides are available from `https://github.com/kristinemlarson/gnssrefl`

The package allows downloading either RINEX or SNR daily files (hereinafter $SNR-ready$) from global archives of GNSS data (e.g. UNAVCO, NGS, BKG) for format conversion, reflector height computation, data assessment, as well as producing daily or subdaily solutions of reflector height. It provides support for formats RINEX versions 2.11 (Gurtner & Estey, 2007a) and 3.00 (Gurtner & Estey, 2007b) as well as NMEA (NMEA, 2018).

The SNR data used for the real-time simulation at the tested sites TGMX, CALC, and GWES were obtained through the *gnssrefl* package by using the command $rnx2snr$ that directly gives $SNR-ready$ files by providing the station name, year, Day of the year (DOY) of the desired data and other optional information. The station name format varies depending on the RINEX version stored. For the TGMX and CALC, the RINEX version is 2, so the station name is lowercase four-character (tgmx, cacl). On the other hand, GWES is RINEX 3 version, so the station name is lowercase nine-character (gwes00deu). In the case of data measured at WESL and BEUE stations, the measurements collected by PRP devices in format NMEA were directly obtained and translated to $SNR-ready$ files using the utility $nmea2snr$.

The $SNR-ready$ files contain information such as satellite ID, SNR observed, time stamp, and satellite azimuth and elevation angle. The azimuth and elevation angle are used to determine the data that comes from sensing zones that are reflected only on the surface of the water. The *gnssrefl* package contains the $quickLook$ and $refl_zones$ utilities, as well as the Reflections Zones online service (`https://gnss-reflections.org/rzones`) are useful tools to estimate the azimuth and elevation angle mask by visualizing the reflection footprints and level height estimations computed with LSP method. Once the reflection zones are defined, the $SNR-ready$ data can be used to simulate water level in real-time through the implementation previously described in the sub-section 2.3.

The co-located tide gauge data from a specific data set (e.g. NOAA, UNESCO) can be

also obtained through the *gnssrefl* package by using the utility other software utilities (see `https://pypi.org/project/gnssrefl`). For site TGMX, the utility *download_ioc* was used by using the station name "pumo2" and the desired time. In CALC, the utility *download_tide* was used by using the station id "8768094" and the desired time.

Chapter 4

Results and Discussion

This chapter covers the results derived by implementing the procedure described in the sub-chapter 2.3. The resulting water levels are evaluated by comparing them to co-located tide or river gauges water level series. Two coastal sites (TGMX and CALC) were used to assess the real-time sea level monitoring and the detection of storm surges, while real-time river level monitoring and river flood detection were evaluated in three river bank sites (GWES, WESL, and BEUE). At the same time, in the river bank sites (WESL and BEUE), it is explored the use of low-cost antenna data as a data source for river level monitoring in real-time.

4.1 Real-time sea level monitoring

In this sub-chapter, the real-time GNSS-IR implementation is assessed for sea level monitoring. The analysis includes exploring the impact of the reflecting zone size on the performance of the implementation.

The test sites TGMX (3.1.1) and CALC (3.1.2) were selected as the two are sites with GNSS stations that records GPS, GLONASS, and Galileo in time intervals of 15 seconds and have a clear line of sight in the direction of the sea surface. The TGMX site has a line of sight that allows a reflection zone that covers 160° between its azimuthal limits (see Figure 3.1.1.1). This means that almost 50% of the azimuthal directions where it is possible to observe GNSS data is available. In terms of the elevation angles, the reflecting zone has good coverage at low angles. However, reflections from larger angles ($> 20°$) were not used to avoid interference in the reflected signal that may be caused

by the dock, especially in the south direction. The CALC site also has a GNSS antenna with a clear line of sight in the direction of the sea surface (see Figure 3.1.2.1). The reflecting zone coverage is over 45% of the available horizontal directions with azimuthal limits of 190° to 340°, mainly limited by the shape of the shore. The elevation angles have good coverage that includes angles between 4° to 25°. This combination of multi-GNSS antenna together with a wide reflection zone allows both sites to have observations almost continuously, presenting only brief intervals with missing data that generally did not exceed 10 minutes. Figure 4.1.1.1 (a) shows the number of observations every 15 seconds during 24 hours of measurement on February 16th, 2022 in TGMX, where it is possible to observe time instants with more than 20 observations simultaneously. Notice that the number of observations does not mean the number of satellites observed, since a single satellite transmitting various frequencies generates multiple measurements at the same time.
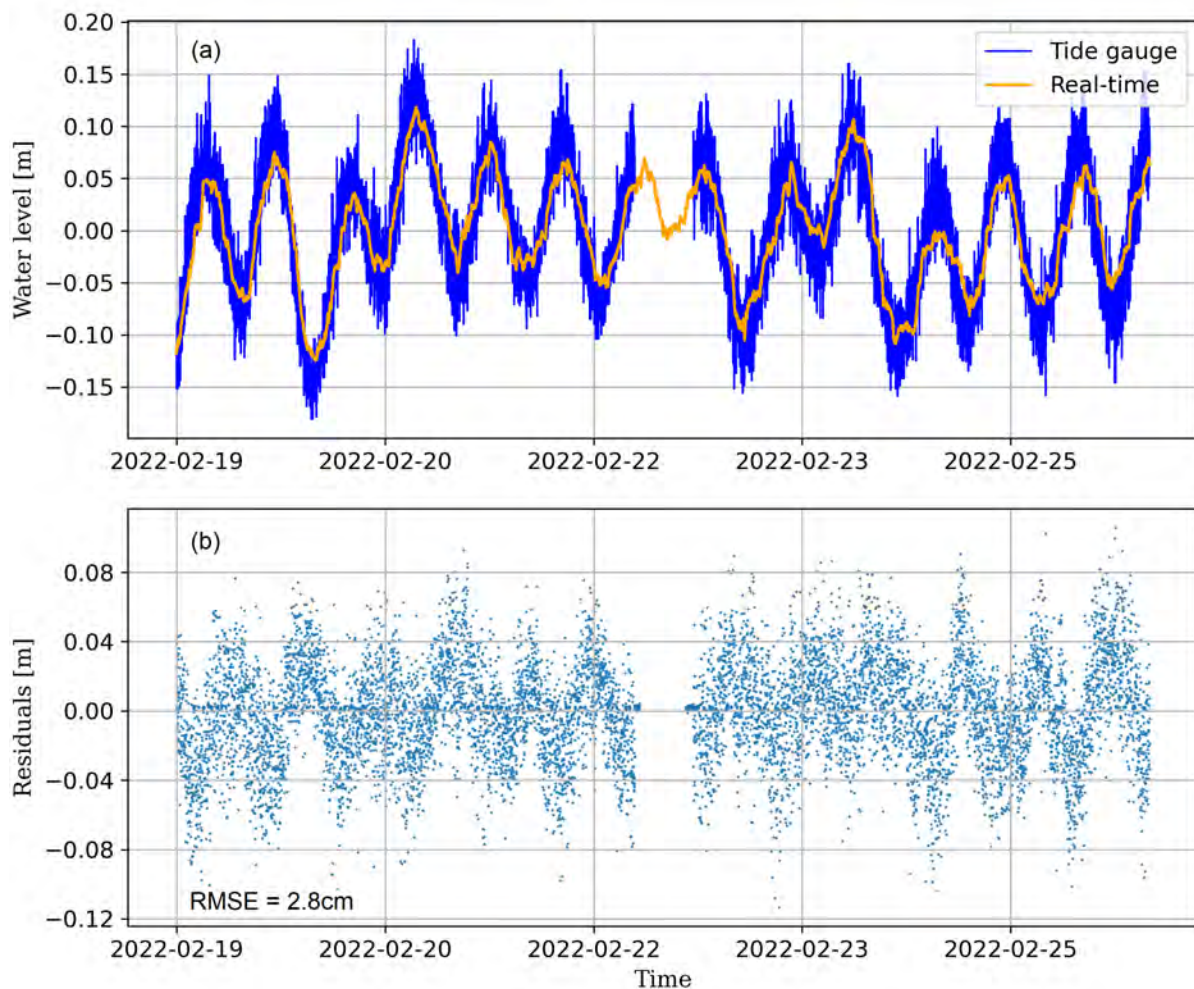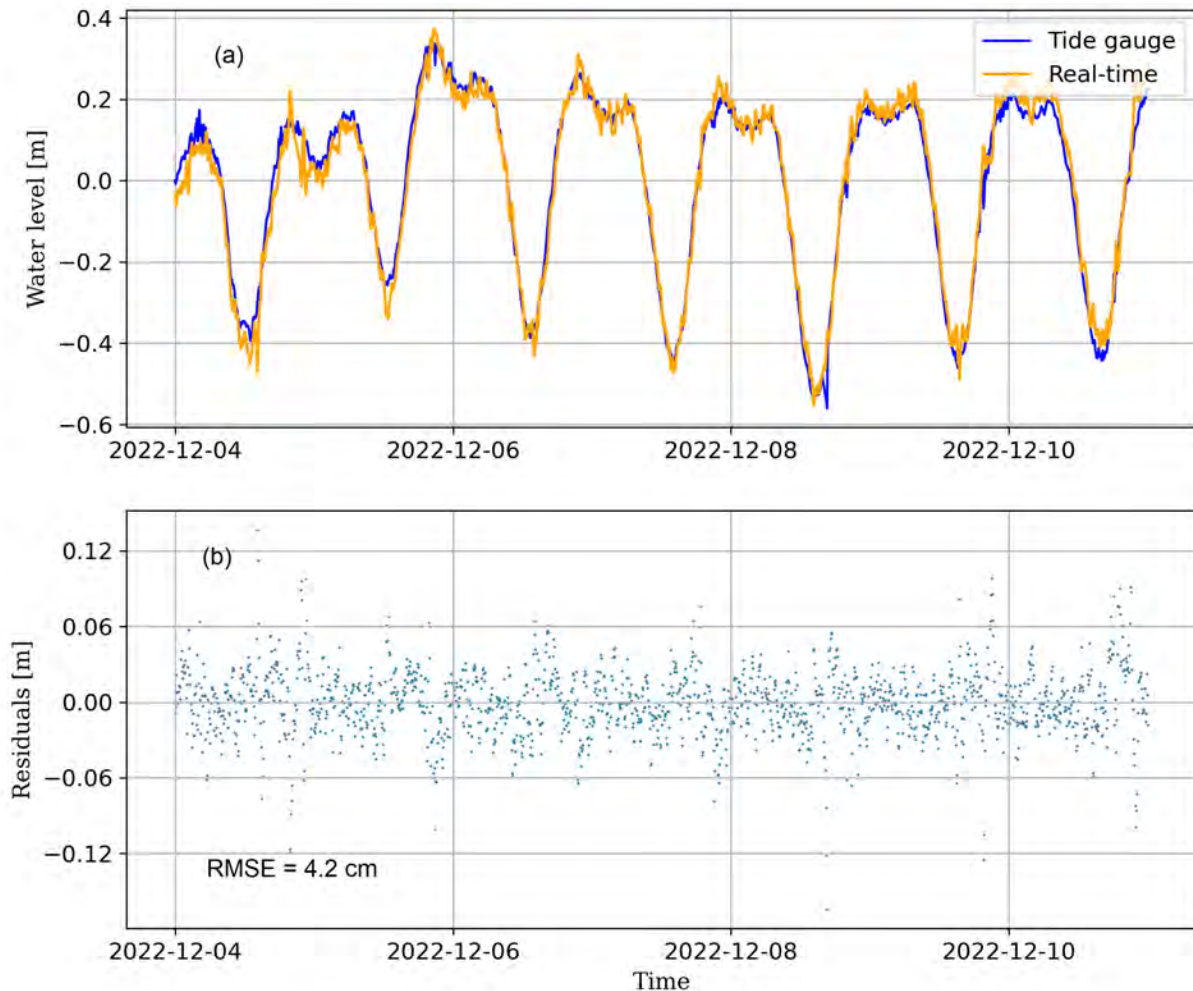

Figure 4.1.0.1: (a) Time series of one-week sea level from the TGMX site tide gauge and real-time GNSS-IR retrievals. The mean was eliminated to enable comparison. (b) Residuals as the difference between GNSS-IR retrievals and tide gauge records.

Table 4.1: System noise parameters used in the EnKF in TGMX and CALC.

Parameter	TGMX	CALC
h	$1x10^{-7}m^2/s$	$1x10^{-6}m^2/s$
A	$1x10^{-7}(V/V)^2/s$	$1x10^{-6}(V/V)^2/s$
φ	$1x10^{-11}rad^2/s$	$1x10^{-11}rad^2/s$
Λ	$1x10^{-11}/s$	$1x10^{-10}/s$

The system noise parameters used are shown in Table 4.1. Since there is a lack of specific information regarding the variables that could affect the SNR and how they changed over time, the estimation of these parameters was done through empirical testing. The system noise of the phase delay φ was imposed to have a small value since rapid changes in the SNR related to sudden water level changes can be interpreted as phase changes of the signal. The height noise was approximated based on the sea level variations observed when the slope is maximum. For example, in TGMX the used value is the square of an expected level change of 0.3 mm/s. The damping factor also has a small associated system noise, which allows the filter to estimate changes in sea level in the presence of changes in the reflecting surface, e.g. changes in surface roughness. However, it is necessary to be careful when estimating this value, since other external factors that can affect the signal strength can also attenuate the signal, causing the filter to be unable to estimate heights in the presence of rapid changes.

In TGMX real-time sea level estimation was computed from thirty days of measurements from February 12th to March 14th, 2022, using all the available observations and the previously mentioned reflection zone. The EnKF in this implementation was initialized with an amplitude of 50 $Volt$ (same for all initial A) and a damping coefficient of 0.01 and the measurement noise was estimated as 300 $Volts^2$.

The implementation was first run using GNSS data with a frequency of 15 seconds. A subset of seven days of the tide gauge records and real-time GNSS-IR solution is presented in Figure 4.1.0.1 (a). The tide gauge data used have a time rate of one minute, therefore, the GNSS-IR solution was averaged to equal the sample rate by computing the mean of all the available data in every minute and the mean of the time series was removed to compare the water level variations. As a result, the GNSS-IR real-time solution showed a RMSE of 2.8 cm. The residuals (Figure 4.1.0.1 (b)) showed a good performance of the real-time solution, with more than 90% of the residuals smaller than 5 cm. The high-frequency variation noticed in the tide gauge time series is due to the fact that the radar sensor is installed outdoors and its measurements are affected by near-shore waves. The variation introduced by the swell has a greater effect on the tide gauge measurements than

on the real-time solution because the footprint of the radar sensor on the sea surface is much smaller than the area over which the signals used in GNSS-IR are reflected, causing the tide gauge observations to be relatively noisier than the real-time solution.

Figure 4.1.0.2: (a) Time series of one-week sea level from the CALC site tide gauge and real-time GNSS-IR retrievals. The mean was eliminated to enable comparison. (b) Residuals as the difference between GNSS-IR retrievals and tide gauge records.

The implementation was again run using 30-second frequency SNR data. The resulting time series showed the same RMSE previously obtained with the 15-second frequency data. The similarity of the solutions can be explained by the low-range tidal variations observed in the TGMX site during the study period. The sea level variations in TGMX are dominated by sub-daily tides, usually with magnitudes of 20 *cm*, with periods close to 6 hours, and maximum changes of 45 *cm*. Meaning that, in time intervals of 15 or 30 seconds, water level variations of less than a few millimeters are expected. Hence, the EnKF is able to estimate solutions with similar accuracy using any of the two sample

rates.

In Figure 4.1.0.1 (a) it is also possible to appreciate a period of about six hours in which the tide gauge was out of service while the GNSS device continued measuring. Therefore, based on the RMSE results, it is possible to indicate that the GNSS-IR solution obtained in TGMX could be used in order to recover that missing sea level data with equivalent accuracy to the one obtained by the tide gauge measurements.

The real-time sea level estimation in CALC was computed from nineteen days of measurements from November 22th to December 10th, 2022, using all the available observations and the previously mentioned reflection zone. The time interval used to test the implementation in real time was limited by the availability of consecutive data with a measurement frequency of 15 seconds. The EnKF was initialized with an amplitude of 60 $Volt$ (same for all initial A) and a damping coefficient of 0.01 and the measurement noise was estimated as 400 $Volts^2$.

Figure 4.1.0.2 (a) shows a subset of seven days of the tide gauge records and real-time GNSS-IR solution run using SNR data with a 15-seconds frequency. The tide gauge data used have a time rate of one minute, therefore, the GNSS-IR solution was averaged to equal the sample rate and the mean of the time series was removed. Unlike the TGMX tide gauge data, in CALC the water level measurements are not affected by high-frequency disturbances, so less noise is observed in the time series.

The GNSS-IR real-time solution using 15-second frequency data showed a RMSE of 4.2 cm. More than 85% of the residuals were lower than 5 cm, indicating that the real-time solution performed well (see Figure 4.1.0.2 (b)). By using 30-second frequency SNR data it was obtained the same RMSE. As in TGMX, this can be explained by due to the sea level variations in CALC are dominated by diurnal tides, and influenced by runoff from Lake Calcasieu, with magnitudes in the order of 120 cm. This means that the variations expected in time intervals of 15 or 30 seconds are less than a few millimeters. Therefore, the EnKF is capable of estimating solutions with similar precision using either of the two sampling frequencies.

4.1.1 Reflecting zone size impact

As was mentioned in sub-Chapter 1.3.3, the size of the reflection zone strongly determines the number of satellites that can be observed by the device during the measurement.
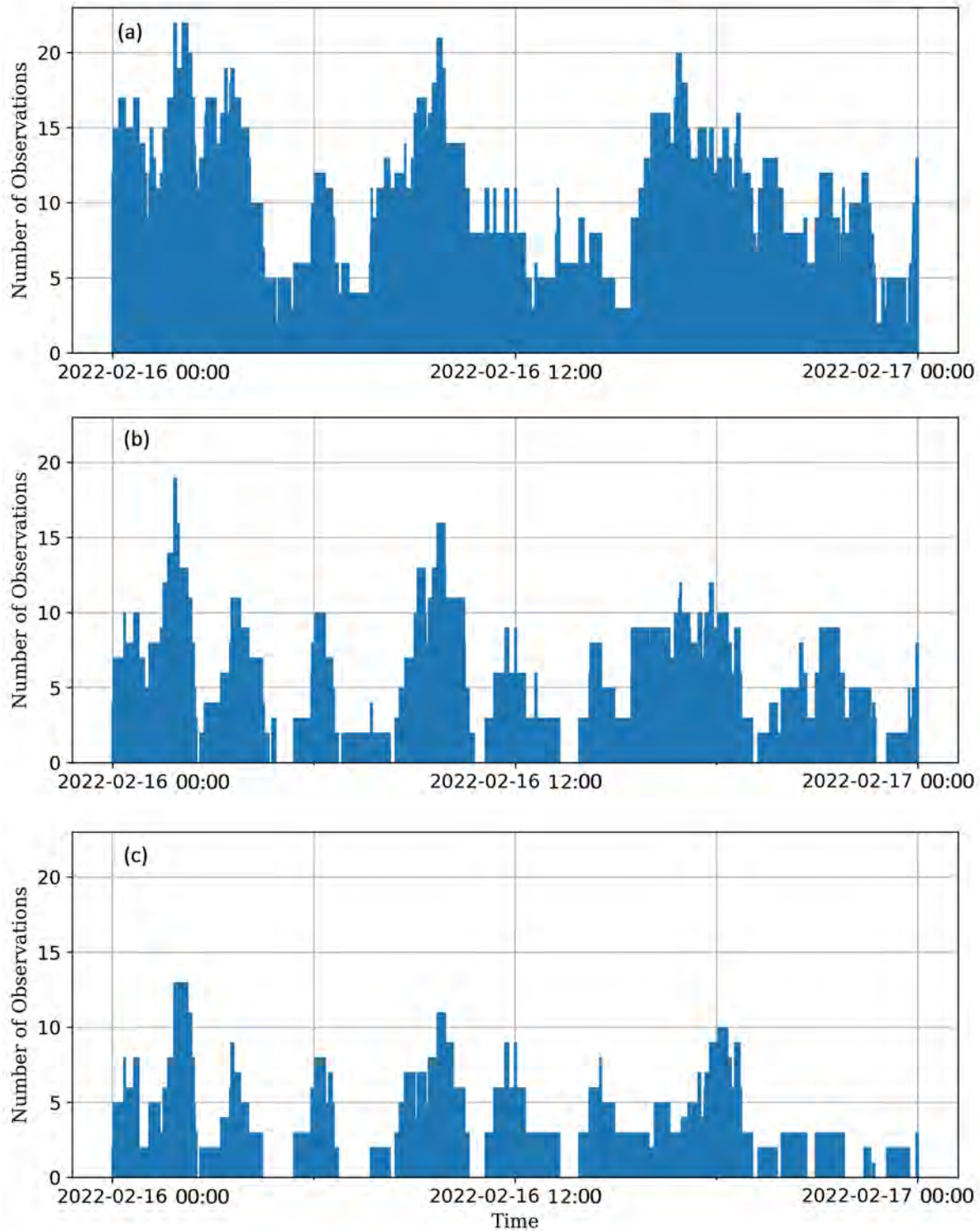
Figure 4.1.1.1: Number of measurements per time instant at TGMX test site on February 12th, 2022. (a) The number of measurements using reflection zones corresponding to azimuth 30°–190° and elevation 4°-20°. (b) The number of measurements using reflection zones corresponding to azimuth 84°–190° and elevation 4°-20°. (c) The number of measurements using reflection zones corresponding to azimuth 137°–190° and elevation 4°-20°.
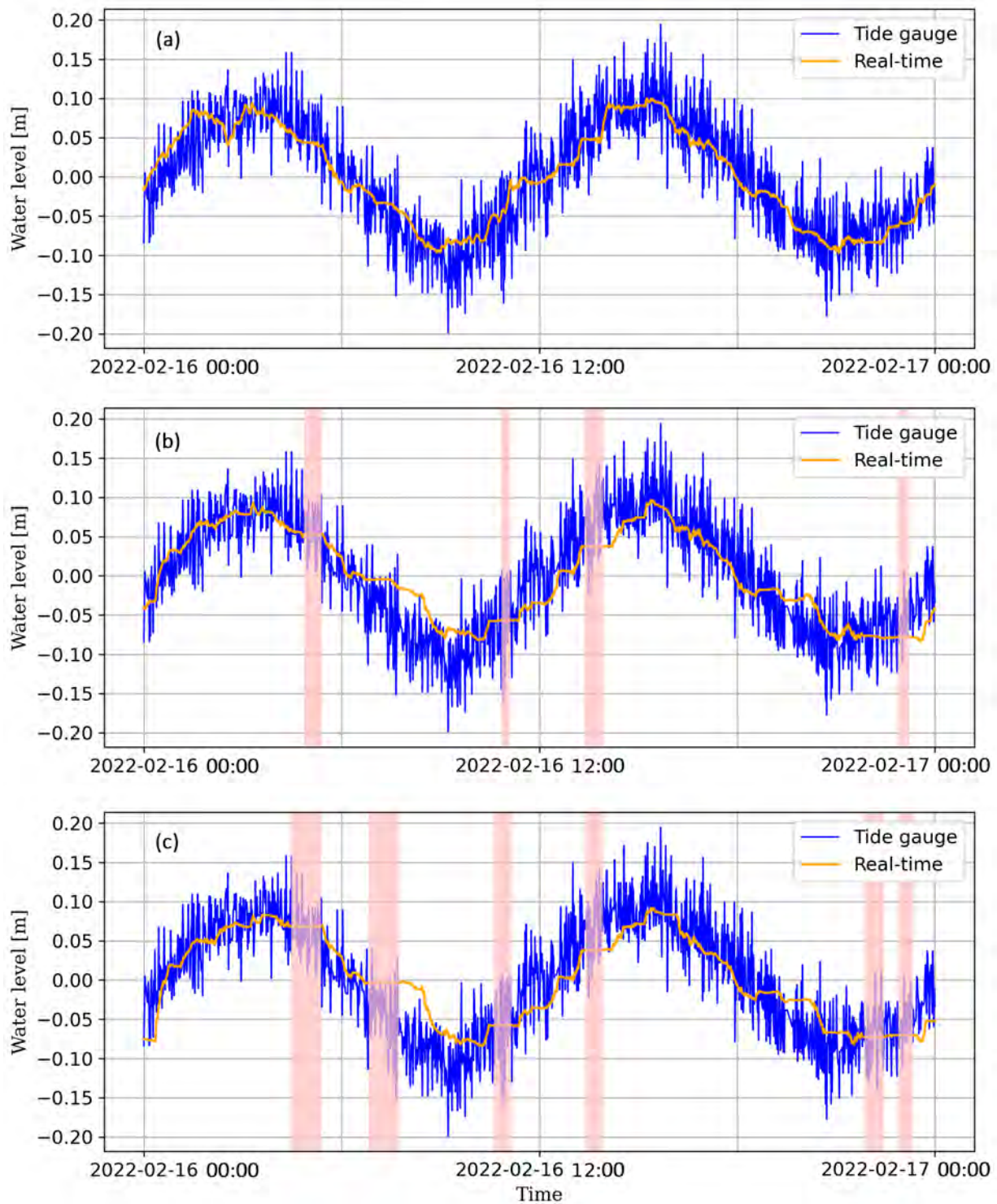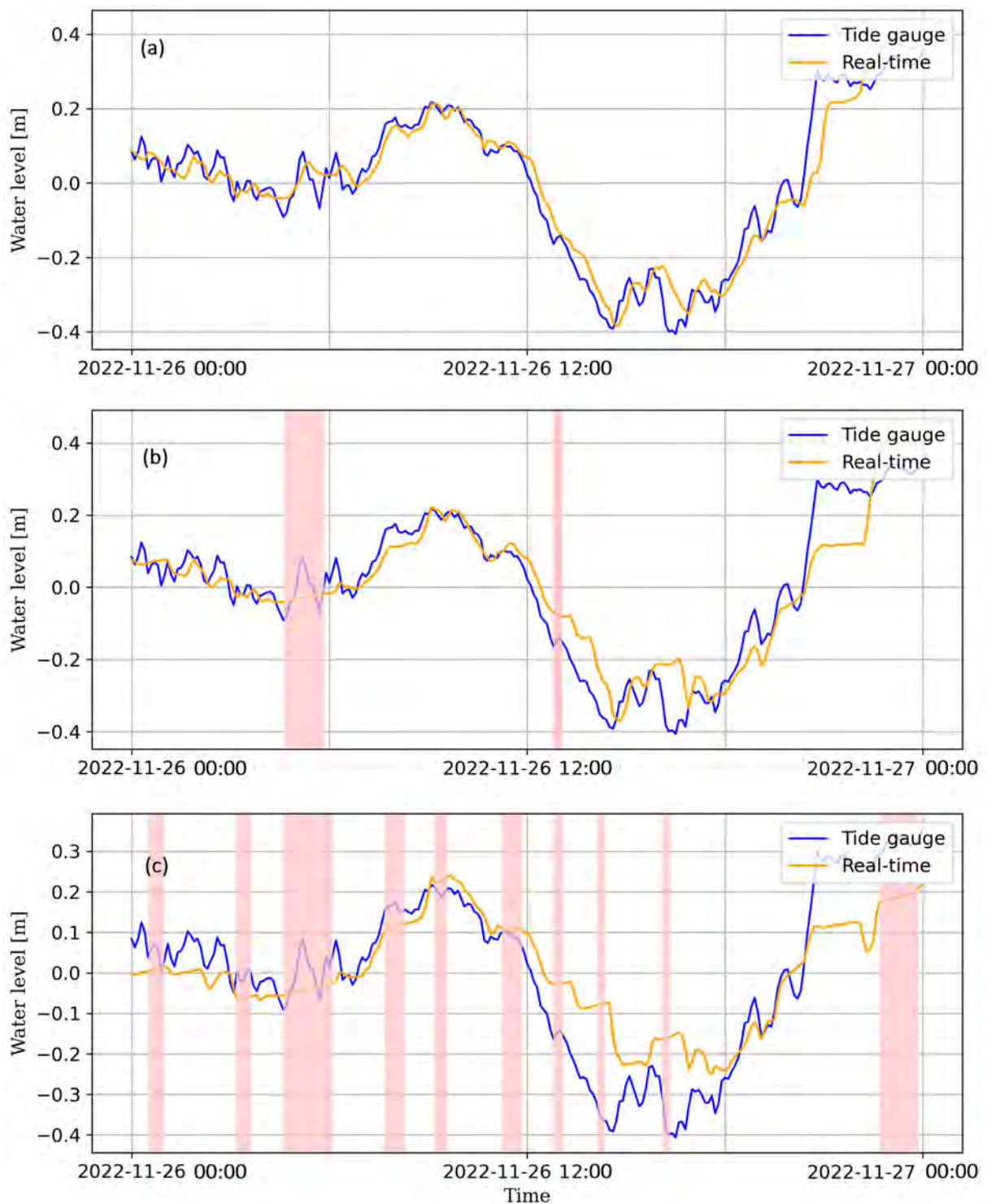
Figure 4.1.1.2: Time series of one-day sea level from the TGMX site tide gauge and real-time GNSS-IR retrievals on February 12th, 2022. The highlighted sections indicate the presence of missing data greater than 30 min. (a) Result using reflection zones corresponding to azimuth 30°–190° and elevation 4°-20°. (b) Result using reflection zones corresponding to azimuth 84°–190° and elevation 4°-20°. (c) Result using reflection zones corresponding to azimuth 137°–190° and elevation 4°-20°.
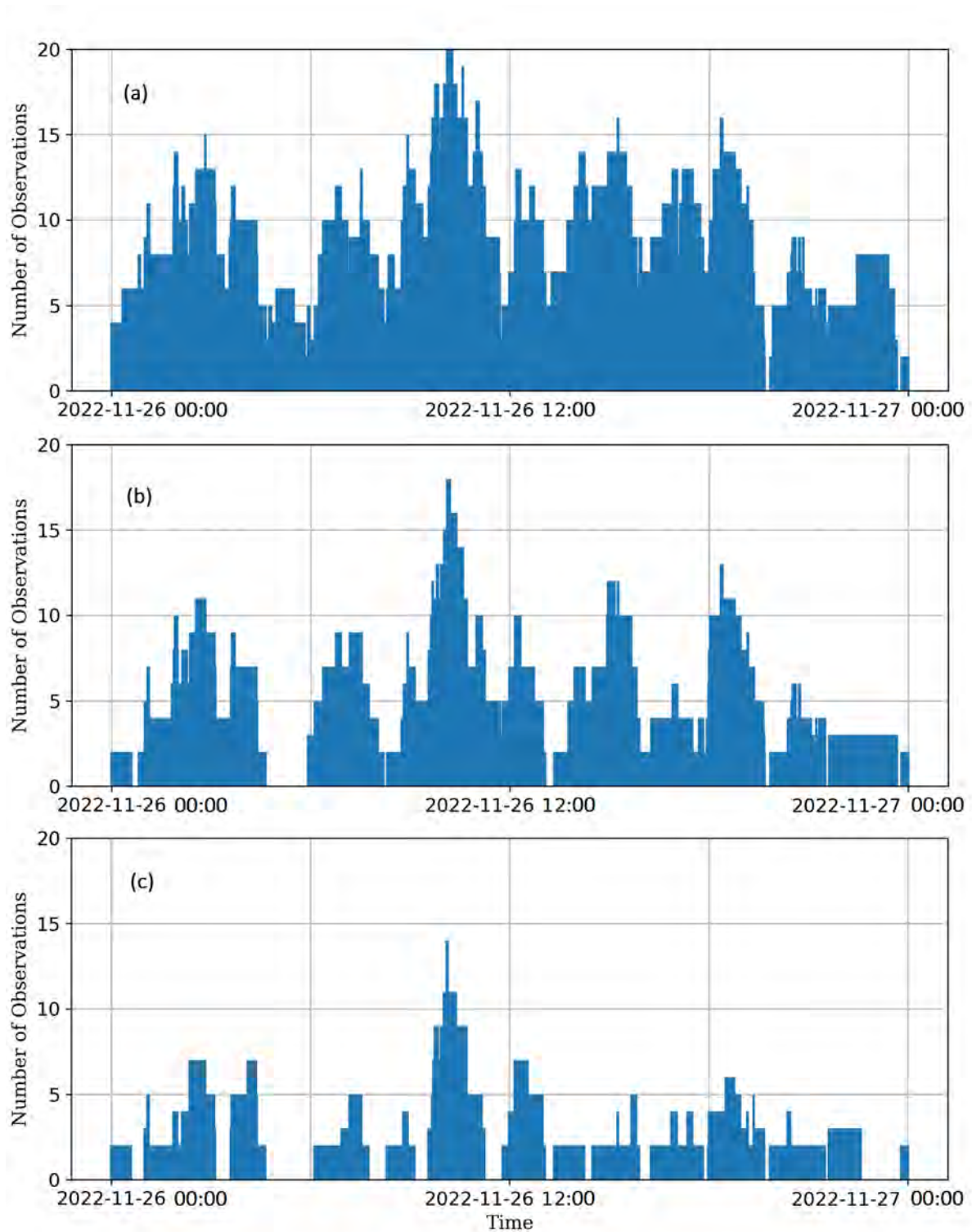
Figure 4.1.1.3: Number of measurements per time instant at CALC test site on November 26th, 2022. (a) The number of measurements using reflection zones corresponding to azimuth 190°–340° and elevation 4°-25°. (b) The number of measurements using reflection zones corresponding to azimuth 190°–290° and elevation 4°-25°. (c) The number of measurements using reflection zones corresponding to azimuth 190°–240° and elevation 4°-25°.

Figure 4.1.1.4: Time series of one-day sea level from the CALC site tide gauge and real-time GNSS-IR retrievals on November 26th, 2022. The highlighted sections indicate the presence of missing data greater than 30 $min.$ (a) The number of measurements using reflection zones corresponding to azimuth 190°–340° and elevation 4°-25°. (b) The number of measurements using reflection zones corresponding to azimuth 190°–290° and elevation 4°-25°. (c) The number of measurements using reflection zones corresponding to azimuth 190°–240° and elevation 4°-25°.

A small reflection area may result in no measurements for certain periods of time, during which the EnKF cannot update the state vector.

The impact of missing data related to the established limits for the reflection zone was evaluated by reducing the azimuthal mask limit to the range 84°-190° and the range 137°-190° in TGMX and to 190°-290° and the range 190°-240° in CALC. Figure 4.1.1.1 (b) and (c) shows how the number of observed data decreases when the reflecting zone was decreased in TGXM. When the limits of the azimuthal mask are changed to 84°-190°, multiple time intervals up to 47 *min* in which there are no observations appear, and reaching time spans up to 112 *min* and increasing in number when the reflection area was limited to the range of 137°-190°.

In the case of CALC, the maximum duration of the intervals without observations were up to 38 and 89 *min* respectively when reducing the azimuthal limits, and, as can be inferred in Figure 4.1.1.3 (b) and (c), the frequency with which these intervals appear increased significantly.

The time intervals without observations translate into intervals in which the EnKF cannot update the state vector, causing the water surface to remain unchanged (due to the assumption in the prediction step of the filter). This effect can be seen in Figure 4.1.1.1, where the highlighted sections in (b) and (c) indicate time intervals within a constant filter solution, causing the filter solution to drift away from the actual water surface level.

Similarly, during the time with no observations, the EnKF adds system noise at each prediction step without an update step to decrease it, steadily increasing the uncertainty of the state vector elements. This causes the error in the water level estimation to spread to subsequent solutions to the missing data.

The resulting RMSE values obtained after running the implementation using 15-second frequency SNR data and the aforementioned azimuthal mask in TGMX were 4.1 and 4.8 *cm* respectively. The intervals without data caused the appearance of differences between the estimation of EnKF and the observation of the tide gauge that reached up to 22 *cm*. On the other hand, in CALC, the errors reached resulted in the divergence of the EnKF estimation, making it not possible to implement real-time monitoring when the azimuthal mask of 190°-240° was used. With this exercise, it was determined that the divergence of the filter occurs when the difference between the estimated water level and the actual level differ in magnitudes close to 40 *cm*. Therefore, it is possible to conclude that the presence of long intervals without measurements does not allow real-time monitoring of the water surface level using the GNSS-IR technique in places where large level variations

are expected in short periods of time, as well as the monitoring of rapid changes in sea level such as those related to atmospheric phenomena or seismicity. At the same time, it highlights the great importance of the study and determination of the reflection zones for real-time sea level monitoring with GNSS-IR.

4.1.2   Coastal storm surges monitoring

The Spectral Analysis method, which is a post-processing implementation of GNSS-IR, has proven useful in storm surge monitoring. Real-time GNSS-IR has proven to be a potential tool for sea level monitoring, thus its usefulness for storm surges observation was explored in this sub-chapter.

A storm surge is an exceptional rise in the water level that exceeds the predicted astronomical tides. They are primarily brought on by powerful winds from hurricanes or tropical storms that push the water toward the shore causing potentially destructive coastal flooding.

The study was carried out with data collected at the site CALC in 2017 and 2020. Between August 25th and 29th, 2017, Hurricane Harvey moved through the area of the Gulf of Mexico generating storm surges that hit a large part of the southern coast of the United States of America, including the Louisiana coast where CALC is located. While in the period from August 26th to August 28th, 2020, Hurricane Laura passed directly over the CALC site. Allowing the influence of these atmospheric phenomena on the sea level to be measured on both occasions.

The EnKF implementation was run with 30-second frequency SNR data, using all the available observations (constellations and frequencies). The filter was initialized with an amplitude *A* of 60 *Volt* and a damping coefficient of 0.01. The system noise parameters used are shown in Table 4.1.

As shown in Figure 4.1.2.1 (a), the water level estimated by the EnKF had a good performance obtaining an RMSE of 4.4 *cm*, the same precision achieved at that site when monitoring sea level under normal conditions. An increase in the magnitude of the residuals was observed during the time that the water level was altered by the storm (see Figure 4.1.2.1 (b)), which can be related to an increase in the variability of the water surface that influences the GNSS antenna measurements, but does not affect the measurements of the tide gauge, which is protected from external influences inside the

structure in which it is installed. Despite this, the filter estimates remained within a range of less than 5 *cm* about 85% of the time, with the largest differences being related to periods with missing SNR data.
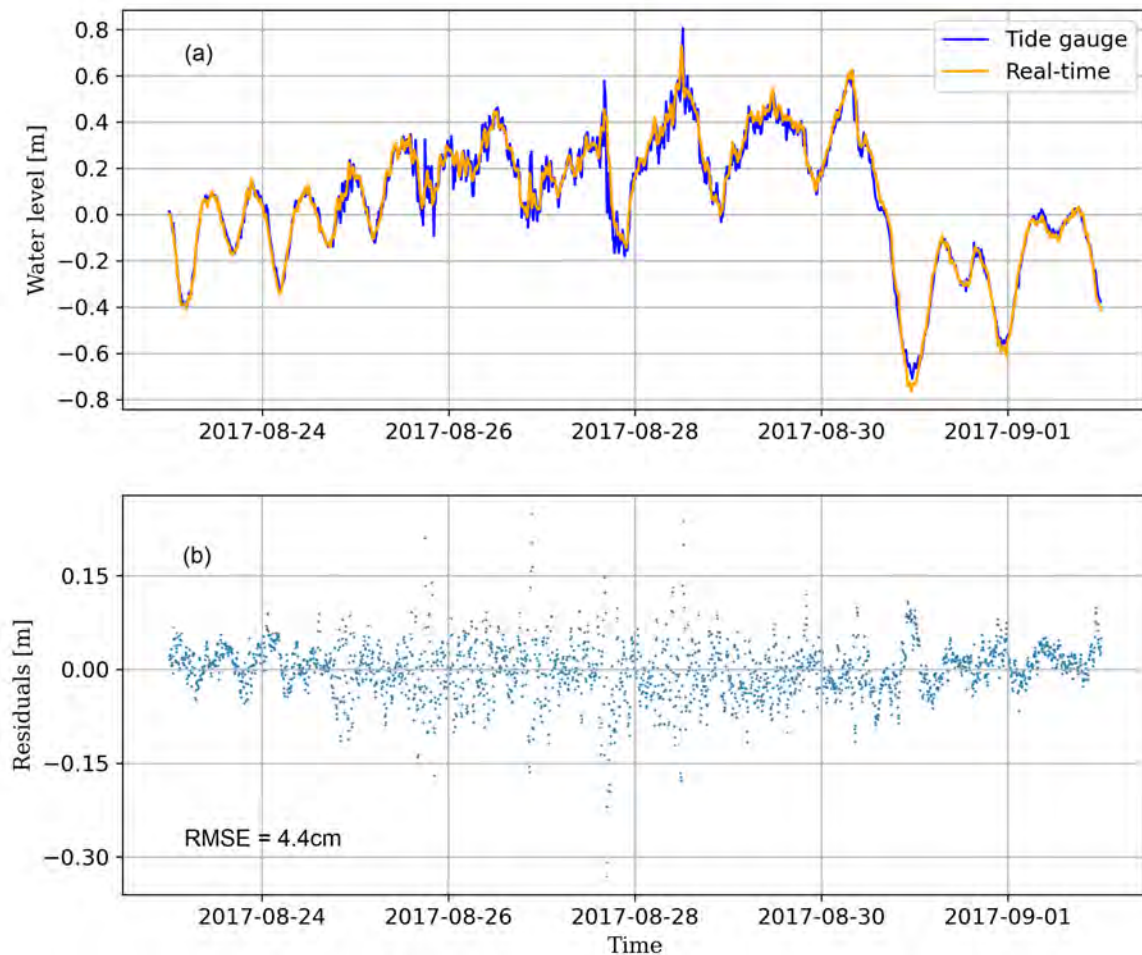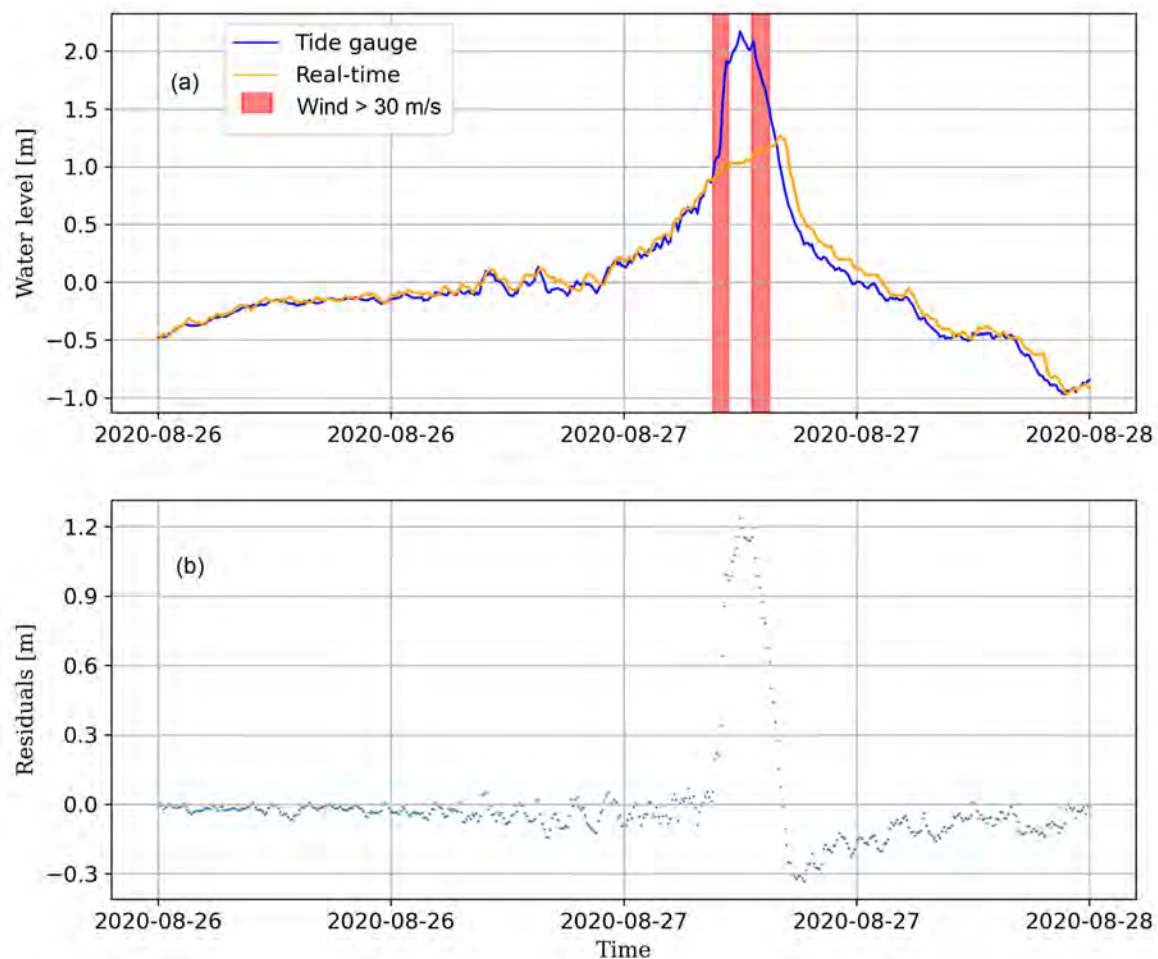

Figure 4.1.2.1: (a) Time series of nine days of sea level from the CALC site tide gauge and real-time GNSS-IR retrievals that monitored the storm surges caused by Hurricane Harvey in 2017. The mean was eliminated to enable comparison. (b) Residuals as the difference between GNSS-IR retrievals and tide gauge records.

When monitoring the effect of Hurricane Laura it was found that the water level estimated by the EnKF had a good performance until the winds caused by the hurricane reached speeds higher than 30 *m/s*. This is shown in Figure 4.1.2.2 (a), denoted with red bars. The strong winds cause an increase in the roughness of the water surface as a consequence of the increasing significant wave height.

The decrease of the specular reflection reduces the amplitude of the SNR oscillating part, which depends on both the direct and the reflected signals. In principle, this reduction

in signal amplitude could be assimilated by the filter by adapting the parameters of the state vector with each new measurement. However, most of the reflected signal that is still detected by the antenna is reflected from the crests of the waves, whose height varies continuously, causing the frequency of the oscillating part of SNR to also vary rapidly and continues, causing the filter to not be able to adapt the state vector parameters efficiently, and ultimately causing it to diverge.

Similar results were obtained by Larson et al. (2021), where it was determined that the reliability of the post-processing GNSS-IR Spectral Analysis method is maintained until the sea surface roughness inhibits coherent specular reflection.

Figure 4.1.2.2: (a) Time series of two days of sea level from the CALC site tide gauge and real-time GNSS-IR retrievals that monitored the storm surges caused by Hurricane Laura in 2020. The red bars represent periods where the wind speed was larger than 30 m/s. The mean was eliminated to enable comparison. (b) Residuals as the difference between GNSS-IR retrievals and tide gauge records.

The passage of the hurricane's eye over the CALC location is represented by the time

between the two red bars. During this time, both wind speed and ocean surface roughness decreased. Regardless, the difference between the exact water level (as indicated by the tide gauge) and the filter estimate at the time was more than one meter (see Figure 4.1.2.2 (b)). This difference is substantially greater than what the filter can assimilate as a change in water level, hence no improvement in water level estimation occurred during that interval. However, after the storm, the water level dropped closer to the filter estimate and the solution began to converge again to a more correct result. The residual did not diminish rapidly after the passage of the storm because the filter required time to re-estimate all elements of the state vector, whose values were accumulating uncertainty throughout the time the estimates were affected by the high roughness.

4.2   Real-time river level monitoring and flash floods detection

In this sub-chapter, the real-time river level determination with GNSS-IR was explored to assess the capability of the implementation to retrieve river levels, but it also focused on the monitoring of level increases that can cause flooding.

The study was conducted on the site GWES from 31 days of measurements from July 1st to July 31st, 2021, using all the available observations (e.i. GPS, GLONASS, and Galileo) with observations frequency of 30 seconds. The period of time studied is relevant because, during it, significant rainfall drastically increased the level of various bodies of water, inducing flood events. In the case of the Rhine, the river level rose by more than $4.9\ m$. The filter was initialized with an amplitude A of 80 $Volt$ and a damping coefficient of 0.01. The system noise parameters used are shown in Table 4.2.

Table 4.2: System noise parameters used in the EnKF in GWES.

Parameter	Values
h	$1x10^{-6}m^2/s$
A	$1x10^{-7}(V/V)^2/s$
φ	$1x10^{-11}rad^2/s$
Λ	$1x10^{-11}/s$

The site has a clear line of sight in the direction of the river surface. However, as observed in Figure 3.1.3.1 (a), this is limited by the presence of a bridge that does not allow measurements in the southwest quadrant. The reflection zone was delimited to the azimuth

interval 260° to 320° and the elevation angles from 5° to 15°. This small size of the reflection zone results in multiple intervals of up to 90 minutes with no measurements in which the filter cannot update the state vector. Nevertheless, the final result demonstrated that the filter estimation was capable of accurately drawing the level changes before, during, and after the rise of the river level (see Figure 4.2.1.1 (a)). Obtaining a RMSE of 3.7 *cm*.
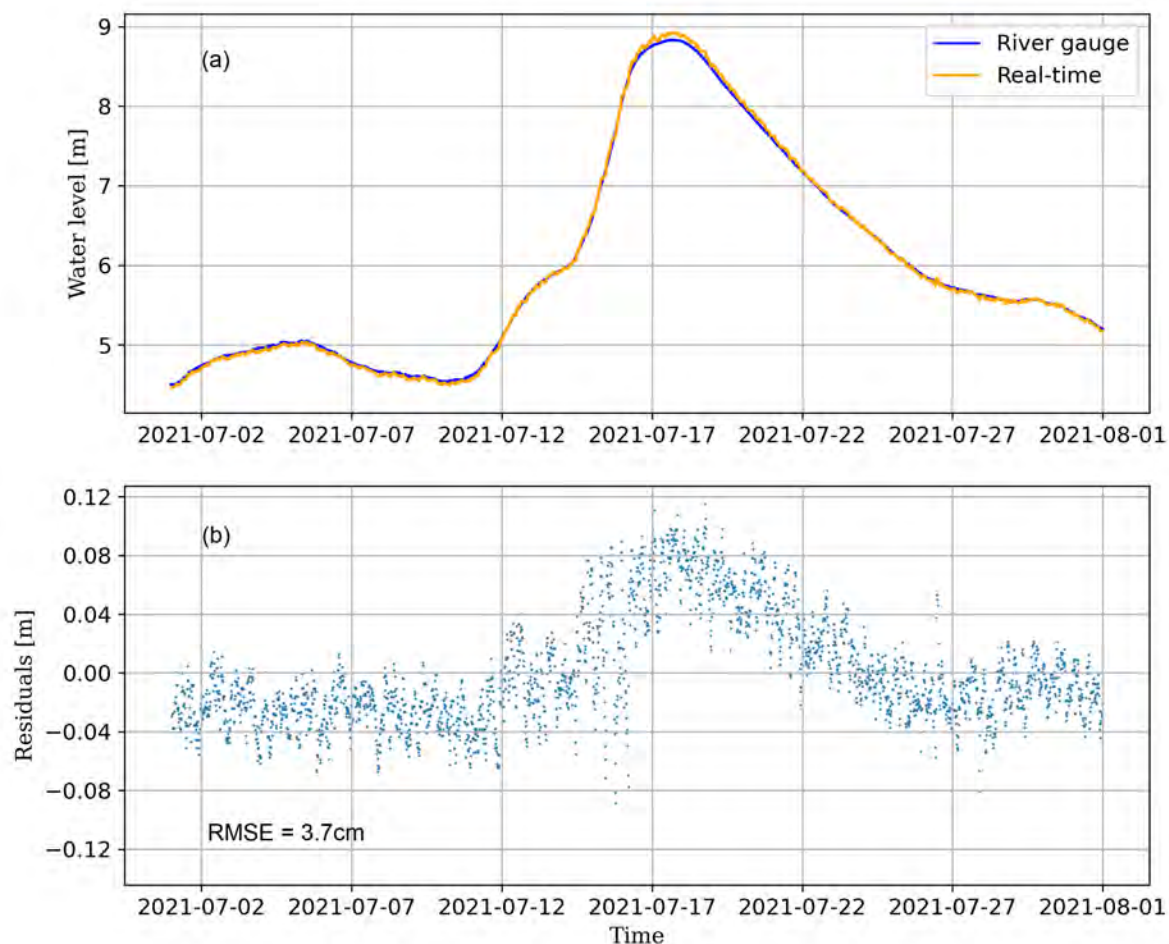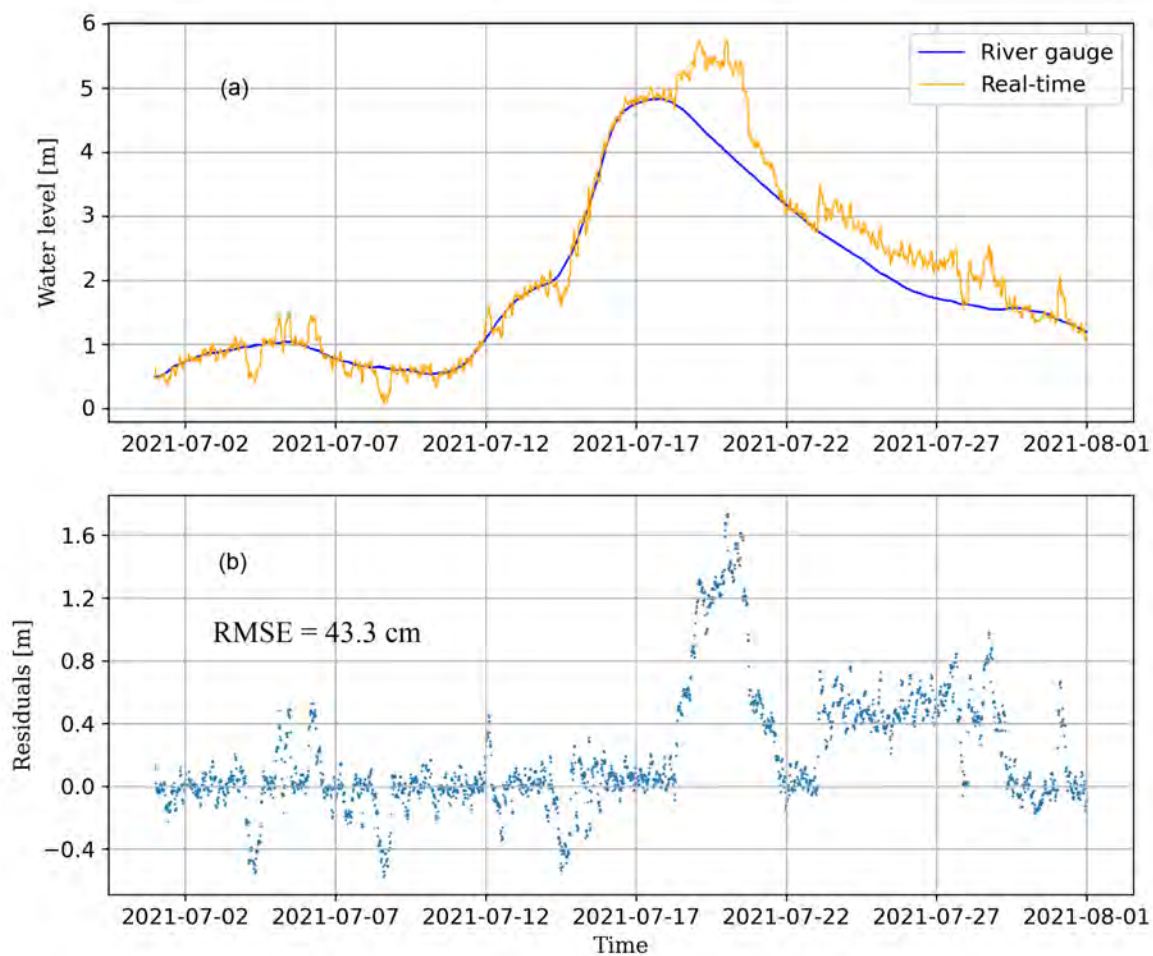

Figure 4.2.0.1: (a) Time series of one-month of river level from the GWES site river gauge and real-time GNSS-IR retrievals. The mean was removed to enable comparison. (b) Residuals as the difference between GNSS-IR retrievals and tide gauge records.

The impact of missing data on the magnitude of the results was most noticeable between July 12th and 17th, when the rate of river level rise was at a maximum (4 *cm/h*). Despite this, the evolution of the residuals in Figure 4.2.1.1 (b) indicates that the filter was able to update the estimates quickly even in the presence of continuous missing data.

In Figure 4.2.1.1 (b) it is also possible to observe a difference between the river gauge and the filter solution that indicates the presence of a bias, whose magnitude increases

as the level of the river subsides and vice versa. When comparing the results obtained only at moments of time in which the river level variations have less magnitude (e.g. July 1st to 12th), the RMSE was reduced to values around 2.0 *cm*. This seems to indicate the existence of a systematic error when comparing the heights estimated with GNSS-IR in real-time with the observations of the pressure sensor installed in the site. The study of this overestimation of the real-time GNSS-IR solution must be studied in more detail, and will ideally require another external data source that allows validating the results of both devices.

4.2.1   Real-time river level monitoring with low-cost antenna

The preceding subchapter highlighted how the real-time GNSS-IR approach can be used to monitor rivers by employing measurements from GNSS antennas capable of receiving multiple satellite constellation signals, even when flood conditions are present. This leads to the question of whether it is possible to use observations obtained with low-cost GPS devices for the real-time monitoring of rivers. Hence, in this sub-chapter, the performance of the EnKF implementation using a PRP (Karegar et al., 2022) instrument data will be assessed.

A PRP instrument was installed in the sites WESL and BEUE in different epochs. In both test sites GPS L1 observations were recorded in time intervals of 1 second (1 *Hz*). However, the SNR data rate was decimated at 30 seconds in order to match the results with what has been previously obtained using more sophisticated GNSS antennas in GWES.

The WESL site shares location with GWES, but the PRP GPS antenna was installed about 3 *m* below the other antenna and a few meters away from it. Therefore, both have a similar line of sight to the river surface, with the same limitations. For this reason, the same azimuth and elevation masks were defined from 260° to 320° and from 5° to 15° respectively.

During its operation in WESL, the PRP instrument was used in two different orientation setups. At first, the GPS antenna was installed in the zenith orientation position (the common way of using GPS for location tasks), while in the second orientation set-up, the antenna was tilted 90° from the vertical direction toward the river with the purpose of increasing the power of the signal reflected on the surface of the river. For this reason, the use of real-time implementation was studied using both data sets separately.

Table 4.3: System noise parameters used in the EnKF in WESL and BEUE.

Parameter	WESL-1	WESL-2	BEUE
h	$1x10^{-5}m^2/s$	$1x10^{-6}m^2/s$	$1x10^{-6}m^2/s$
A	$1x10^{-7}(V/V)^2/s$	$1x10^{-7}(V/V)^2/s$	$1x10^{-7}(V/V)^2/s$
φ	$1x10^{-10}rad^2/s$	$1x10^{-11}rad^2/s$	$1x10^{-11}rad^2/s$
Λ	$1x10^{-12}/s$	$1x10^{-11}/s$	$1x10^{-11}/s$

The first part of the study in WESL was conducted from 31 days of measurements from July 1st to July 31st, 2021, which is the same period used with GWES during which there were heavy rains that caused flooding as a result of the rise of the Rhine river. In this period, the GPS antenna was installed in the zenith orientation position. The filter was initialized with an amplitude A of 57 $Volt$ and a damping coefficient of 0.01. The system noise parameters used are shown in Table 4.3 in column "WESL-1".
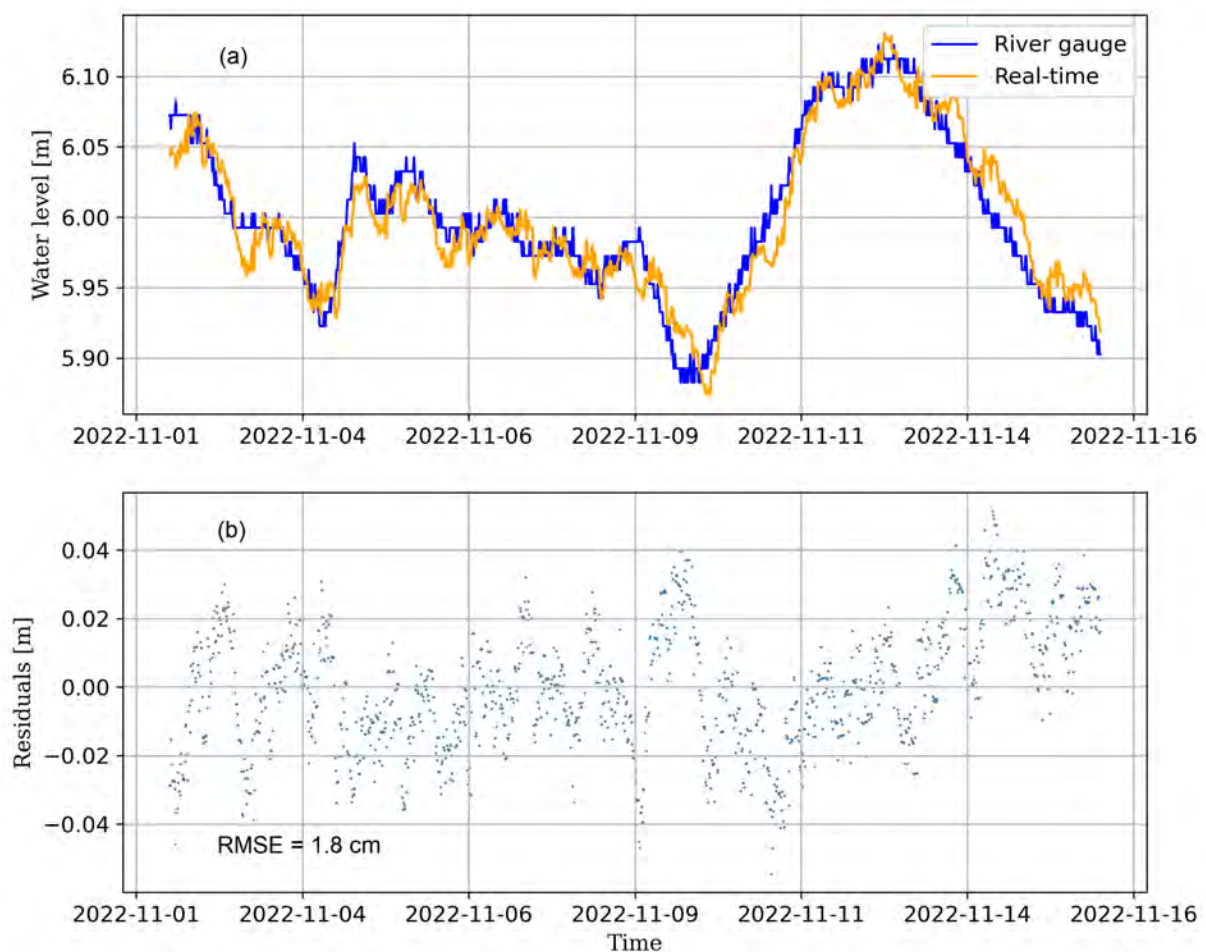

Figure 4.2.1.1: (a) Time series of one-month of river level from the GWES site river gauge and real-time GNSS-IR retrievals. The mean was removed to enable comparison. (b) Residuals as the difference between GNSS-IR retrievals and tide gauge records.

The first implementation in real time showed poor results, in which the filter was not able to follow the variation of the river level accurately (see Figure 4.2.1.1 (a)), showing an RMSE of 43.3 *cm*. For comparison, the data obtained by GWES were processed again but used only the GPS L1 signal using the parameters of Table 4.2, yielding results with an RMSE of 5.6 *cm* (see Figure 4.2.1.2). Both devices were in operation simultaneously, so both tracked the same satellite signals under technically similar ambient and environmental conditions. Hence, it can be intuited that even with a smaller number of data (since only one satellite signal is available) it is possible to obtain precise results. Therefore, in this case, the difference between the results must be mainly related to the capability of each device to measure satellite signals accurately.
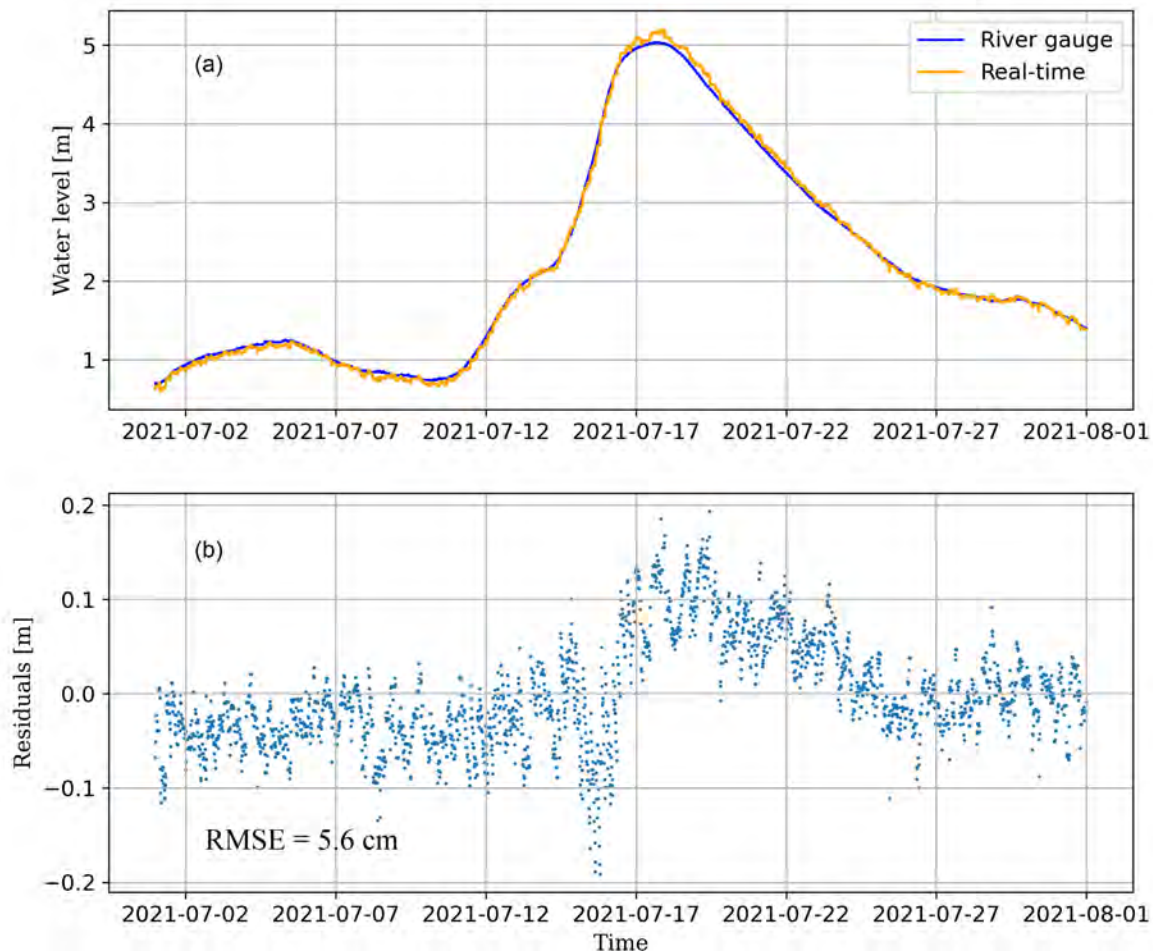
Figure 4.2.1.2: (a) Time series of one-month of river level from the GWES site river gauge and real-time GNSS-IR retrievals. The mean was removed to enable comparison. (b) Residuals as the difference between GNSS-IR retrievals and tide gauge records.

The second experiment of the study in WESL was conducted by using data measured with the PRP instrument GPS antenna installed pointing to the horizon towards the direction

of the river. This change in the orientation of the antenna resulted in an increase in the amplitude of the SNR data and a decrease in noise in it, which strongly impacted the results obtained.
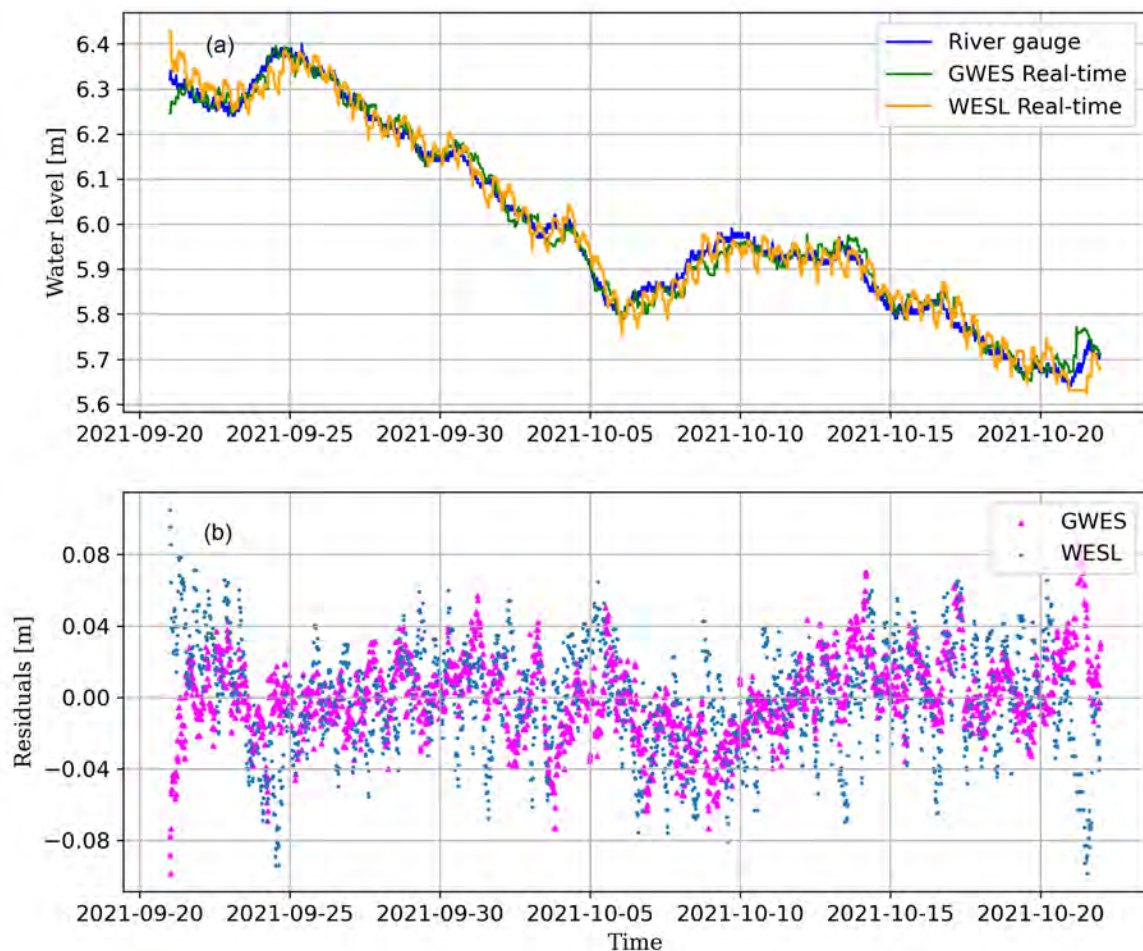
Figure 4.2.1.3: (a) Time series of one-month of river level from the GWES site river gauge and real-time GNSS-IR retrievals. The mean was removed to enable comparison. (b) Residuals as the difference between GNSS-IR retrievals and tide gauge records.

The implementation was tested from September 21st to October 21st, 2021. The filter was initialized with an amplitude A of 150 $Volt$ and a damping coefficient of 0.01. The system noise parameters used are shown in Table 4.3 in column "WESL-2", obtaining a real-time river level solution with a RMSE of 3.0 cm. The results are shown in Figure 4.2.1.3 together with the result obtained using the GWES data, which resulted in an RMSE of 2.2 cm. In contrast to the previous experiment, with the data measured by the PRP GPS antenna pointing to the horizon, the river level estimates improve significantly.

When evaluating the WESL result displayed in Figure 4.2.1.3 (a), it is possible to see a high-frequency variation that is not present in the GWES estimation. These oscillations

could be artifacts created by the filter when using the SNR with enhanced amplitude measured by the GPS antenna of the PRP while tilted toward the horizon. The analysis of this oscillation, however, requires an understanding of the antenna characteristics, such as the antenna gain patterns, and how they influenced the solution given the new pointing configuration.

The same GPS antenna orientation setup was used at the BEUE site, where the PRP instrument was installed to test the real-time river monitoring results that can be obtained with a larger reflecting zone than at the WESL site. The reflection zone at BEUE was limited to an azimuthal range of 140° to 280° and elevation angles of 3° to 20°, implying that the area across which reflections can be perceived is more than twice as wide as the total area available at the WESL site. As a result, the number and duration of time intervals without available measurements were reduced.

Figure 4.2.1.4: (a) Time series of 14 days of river level from the BEUE site river gauge and real-time GNSS-IR retrievals. The mean was removed to enable comparison. (b) Residuals as the difference between GNSS-IR retrievals and tide gauge records.

The implementation was tested from November 2nd to November 15^{ht}, 2022. The filter was initialized with an amplitude A of 190 $Volt$ and a damping coefficient of 0.01. The system noise parameters used are shown in Table 4.3 in column "BEUE", obtaining a real-time river level solution with a RMSE of 1.9 cm. As can be observed in Figure 4.2.1.4 (a) and (b), more than 96% of the residuals are in the interval smaller than 5 cm, indicating that the filter estimation accurately tracked the dynamics of the river level during the days of GPS antenna operation.

With these results, it is feasible to deduce that real-time monitoring of river levels is conceivable using low-cost devices like the PRP instrument when installed so that it points towards the horizon and the water surface. This orientation setup enables the accuracy of the results acquired to be equivalent to that of considerably more complex and expensive geodetic antennas.

Chapter 5

Conclusion and Outlook

The management of water resources, the protection of the environment, the prevention of dangers, and the early warning of floods require control of the water level in real time with monitoring systems capable of measuring variations in the water level accurately while remaining safe and operational during flood events. Consequently, the objective of this thesis was to evaluate water level estimates obtained with GNSS-IR in real time by implementing a Kalman filter.

The Ensemble Kalman Filter (EnKF) was used to build a real-time GNSS-IR water level monitoring system taking advantage of the easy implementation of the EnKF in nonlinear systems that require a state vector with a large number of elements and the possibility to avoid covariance matrix stabilization. The implementation was initially tested in the estimation of the sea level variation by using data obtained by GNSS antennas capable of measuring data from multiple satellite constellations and signals with a measurement rate of 15 and 30 seconds in two different sites. The site TGMX, located in Puerto Morelos, Mexico, and the site CALC, located on the coast of Louisiana, USA. To evaluate the correctness of the real-time solution, sea level records from co-located tidal gauges were used as ground truth sea level. The results showed that the implementation developed in this thesis is capable of monitoring the sea level in sites with moderate tides with a good performance following the dynamics of the ocean with differences between the estimated water height and the reference value is less than 5 cm in more than 90% of the cases, and nearly 100% less than 10 cm. Overall, an RMSE of less than 4.2 cm was achieved. This demonstrates the potential of the developed implementation.

The usage of real-time implementation for storm surge monitoring was examined using GNSS data collected in the site CALC during the passages of Hurricanes Harvey and Laura

on the southern coast of the USA, in 2017 and 2020, respectively. The results provided evidence that variations in water surface roughness can be assimilated by the filter to the point where extreme storm winds minimize the specular reflections by substantially increasing the significant wave height. Therefore, it is appropriate to consider the use of the models applied in the estimation of the significant wave height by means of GNSS-IR as an alternative to improve the performance of the real-time implementation under the previously mentioned challenging conditions.

In the case of river monitoring, the real-time implementation was used with GNSS data measured at the GWES station in Wesel, Germany, which is located on the bank of the Rhine River. The results have shown good performance in monitoring river level variations, including the measurement of flood occurrences, with an RMSE of 3.7 *cm*, evidencing the high accuracy of the water levels estimated by the filter, and demonstrating that real-time river level monitoring can be determined with precision comparable to that obtained with river pressure gauges.

Data from devices that only measure GPS signals at the L1 frequency were used to address the usage of low-cost devices for real-time GNSS-IR monitoring of the river level. The implementation was carried out at the WESL site, located in Wesel, Germany, on the bank of the Rhine River, using data obtained by the instrument in two different orientation setups. The first setup has the GPS antenna pointing toward the zenith, while the second has the antenna pointing toward the horizon and the direction of the river. The results showed that when the low-cost antenna was mounted facing toward the zenith, the river level calculations performed poorly, with RMSE of more than 43 *cm*. Nevertheless, when the antenna was tilted 90° to the vertical, excellent performance was attained with RMSE of 3.0 *cm*. Demonstrating that results comparable to those obtained using data acquired by more expensive and higher-quality antennas can be achieved. These results support the use of low-cost devices as an alternative to monitoring water surfaces with non-intrusive techniques. Exploring the use of low-cost devices capable of measuring multiple constellations and signals is an alternative for future work to test the accuracy of the solution in real-time monitoring of sea and river levels.

The implementation proved to be suitable for real-time monitoring of the dynamics of water surfaces. The filter performance, however, is strongly dependent on the process noise values used in each implementation. The process noise can vary depending on external factors, such as the geometry around the receiver or meteorological conditions. The absence of models that explain the underlying dynamics of the parameters involved in establishing the process noise caused that in this thesis the process noise values were chosen empirically and assumed as constant. Therefore, a more complete study of these

parameters and their dynamics will be a task that can generate an improvement in the results of this implementation.

On the other hand, the simplifications in the measurement model that describes the oscillating part of the SNR cause signal changes associated with the surface and the antenna gain pattern to be mixed in the damping coefficient. Thus, modeling the antenna characteristics together with the Fresnel coefficients in the model function could improve the interpretation of the surface properties.

List of Abbreviations

DOY Day of the year

EKF Extended Kalman filter

EnKF Ensemble Kalman filter

GNSS Global Navigation Satellite System

GNSS-IR GNSS - Interferometric Reflectometry

KF Kalman filter

LSP Lomb-Scargle periodogram

NGS National Geodetic Survey

NOAA National Oceanic and Atmospheric Administration

PRP Raspberry Pi Reflector

RMSE Root-Mean-Square Error

SNR Signal-to-Noise Ratio

SSZ sensing zones

UKF Unscented Kalman filter

UNAVCO University NAVSTAR Consortium

UNESCO United Nations Educational, Scientific and Cultural Organization

ii

List of Figures

List of Tables

x

References

Abdalla, S., Kolahchi, A. A., Ablain, M., Adusumilli, S., Bhowmick, S. A., Alou-Font, E., . . . Zlotnicki, V. (2021, July). Altimetry for the future: Building on 25 years of progress. *Advances in Space Research*, *68*(2), 319–363. Retrieved from `https://doi.org/10.1016/j.asr.2021.01.022` doi: 10.1016/j.asr.2021.01.022

Anderson, K. D. (2000, August). Determination of water level and tides using interferometric observations of GPS signals. *Journal of Atmospheric and Oceanic Technology*, *17*(8), 1118–1127. Retrieved from `https://doi.org/10.1175/1520-0426(2000)017<1118:dowlat>2.0.co;2` doi: 10.1175/1520-0426(2000)017<1118:dowlat>2.0.co;2

Arias, P., Bellouin, N., Coppola, E., Jones, R., Krinner, G., Marotzke, J., . . . Zickfeld, K. (2021). Climate change 2021: The physical science basis. contribution of working group i to the sixth assessment report of the intergovernmental panel on climate change; technical summary. In V. Masson-Delmotte et al. (Eds.), *The intergovernmental panel on climate change ar6*. Retrieved from `https://elib.dlr.de/137584/`

Beckmann, P., & Spizzichino, A. (1987). *The scattering of electromagnetic waves from rough surfaces.*

Bilich, A., & Larson, K. M. (2007, November). Mapping the GPS multipath environment using the signal-to-noise ratio (SNR). *Radio Science*, *42*(6). Retrieved from `https://doi.org/10.1029/2007rs003652` doi: 10.1029/2007rs003652

Crassidis, J. L., & Junkins, J. L. (2011). *Optimal estimation of dynamic systems, second edition* (2nd ed.). Philadelphia, PA: Chapman & Hall/CRC.

Fagundes, M. A. R., Mendonça-Tinti, I., Iescheck, A. L., Akos, D. M., & Geremia-Nievinski, F. (2021, March). An open-source low-cost sensor for SNR-based GNSS reflectometry: design and long-term validation towards sea-level altimetry. *GPS Solutions*, *25*(2). Retrieved from `https://doi.org/10.1007/s10291-021-01087-1` doi: 10.1007/s10291-021-01087-1

Frederikse, T., Landerer, F., Caron, L., Adhikari, S., Parkes, D., Humphrey, V. W., . . . Wu, Y.-H. (2020, August). The causes of sea-level rise since 1900. *Nature*, *584*(7821), 393–397. Retrieved from `https://doi.org/10.1038/s41586-020-2591-3` doi: 10 .1038/s41586-020-2591-3

Georgiadou, P., & Kleusberg, A. (1988). On carrier signal multipath effects in relative gps positioning. *Journal of Geodesy*, *13*(3), 172–179.

Geremia-Nievinski, F., Hobiger, T., Haas, R., Liu, W., Strandberg, J., Tabibi, S., . . . Williams, S. (2020, July). SNR-based GNSS reflectometry for coastal sea-level altimetry: results from the first IAG inter-comparison campaign. *Journal of Geodesy*, *94*(8). Retrieved from `https://doi.org/10.1007/s00190-020-01387-3` doi: 10.1007/s00190-020-01387-3

Gurtner, W., & Estey, L. (2007a, December). *Rinex: The receiver independent exchange format version 2.11.* Bern: Astronomical Institute, University of Bern.

Gurtner, W., & Estey, L. (2007b). *Rinex - the receiver independent exchange format - version 3.00.* Bremerhaven: PANGAEA.

Holden, L. D., & Larson, K. M. (2021, June). Ten years of lake taupō surface height estimates using the GNSS interferometric reflectometry. *Journal of Geodesy*, *95*(7). Retrieved from `https://doi.org/10.1007/s00190-021-01523-7` doi: 10.1007/ s00190-021-01523-7

Julier, S. J., & Uhlmann, J. K. (1997, July). New extension of the kalman filter to nonlinear systems. In I. Kadar (Ed.), *SPIE proceedings.* SPIE. Retrieved from `https:// doi.org/10.1117/12.280797` doi: 10.1117/12.280797

Kalman, R. E. (1960, March). A new approach to linear filtering and prediction problems. *Journal of Basic Engineering*, *82*(1), 35–45. Retrieved from `https://doi.org/10 .1115/1.3662552` doi: 10.1115/1.3662552

Karegar, M. A., & Kusche, J. (2020, Sep). Imprints of covid-19 lockdown on gnss observations: An initial demonstration using gnss interferometric reflectometry. *Geophysical Research Letters*, *47*(19). Retrieved from `http://dx.doi.org/10.1029/2020GL089647` doi: 10.1029/2020gl089647

Karegar, M. A., Kusche, J., Geremia-Nievinski, F., & Larson, K. M. (2022, November). Raspberry pi reflector (RPR): A low-cost water-level monitoring system based on GNSS interferometric reflectometry. *Water Resources Research*, *58*(12). Retrieved from `https://doi.org/10.1029/2021wr031713` doi: 10.1029/2021wr031713

Kim, S.-K., Lee, E., Park, J., & Shin, S. (2021, March). Feasibility analysis of GNSS-reflectometry for monitoring coastal hazards. *Remote Sensing*, *13*(5), 976. Retrieved from `https://doi.org/10.3390/rs13050976` doi: 10.3390/rs13050976

Kim, S.-K., & Park, J. (2021, February). Monitoring a storm surge during hurricane harvey using multi-constellation GNSS-reflectometry. *GPS Solutions*, *25*(2). Retrieved from `https://doi.org/10.1007/s10291-021-01105-2` doi: 10.1007/s10291-021-01105-2

Kirezci, E., Young, I. R., Ranasinghe, R., Muis, S., Nicholls, R. J., Lincke, D., & Hinkel, J. (2020, July). Projections of global-scale extreme sea levels and resulting episodic coastal flooding over the 21st century. *Scientific Reports*, *10*(1). Retrieved from `https://doi.org/10.1038/s41598-020-67736-6` doi: 10.1038/s41598-020-67736-6

Larson, K. M. (2021). *kristinemlarson/gnssrefl: First release.* Zenodo. Retrieved from `https://zenodo.org/record/5601495` doi: 10.5281/ZENODO.5601495

Larson, K. M., Lay, T., Yamazaki, Y., Cheung, K. F., Ye, L., Williams, S. D., & Davis, J. L. (2021, February). Dynamic sea level variation from GNSS: 2020 shumagin earthquake tsunami resonance and hurricane laura. *Geophysical Research Letters*, *48*(4). Retrieved from `https://doi.org/10.1029/2020gl091378` doi: 10.1029/2020gl091378

Larson, K. M., Löfgren, J. S., & Haas, R. (2013, April). Coastal sea level measurements using a single geodetic GPS receiver. *Advances in Space Research*, *51*(8), 1301–1310. Retrieved from `https://doi.org/10.1016/j.asr.2012.04.017` doi: 10.1016/j.asr.2012.04.017

Larson, K. M., Ray, R. D., Nievinski, F. G., & Freymueller, J. T. (2013, September). The accidental tide gauge: A GPS reflection case study from kachemak bay, alaska. *IEEE Geoscience and Remote Sensing Letters*, *10*(5), 1200–1204. Retrieved from `https://doi.org/10.1109/lgrs.2012.2236075` doi: 10.1109/lgrs.2012.2236075

Larson, K. M., Ray, R. D., & Williams, S. D. P. (2017, February). A 10-year comparison of water levels measured with a geodetic GPS receiver versus a conventional tide gauge. *Journal of Atmospheric and Oceanic Technology*, *34*(2), 295–307. Retrieved from `https://doi.org/10.1175/jtech-d-16-0101.1` doi: 10.1175/jtech-d-16-0101.1

Larson, K. M., Small, E. E., Gutmann, E., Bilich, A., Axelrad, P., & Braun, J. (2007, August). Using GPS multipath to measure soil moisture fluctuations: initial results. *GPS Solutions*, *12*(3), 173–177. Retrieved from `https://doi.org/10.1007/s10291-007-0076-6` doi: 10.1007/s10291-007-0076-6

Liu, Z., Du, L., Zhou, P., Wang, X., Zhang, Z., & Liu, Z. (2023, February). Cloud-based near real-time sea level monitoring using GNSS reflectometry. *GPS Solutions*, *27*(2). Retrieved from `https://doi.org/10.1007/s10291-022-01382-5` doi: 10 .1007/s10291-022-01382-5

Ljung, L. (1979, February). Asymptotic behavior of the extended kalman filter as a parameter estimator for linear systems. *IEEE Transactions on Automatic Control*, *24*(1), 36–50. Retrieved from `https://doi.org/10.1109/tac.1979.1101943` doi: 10.1109/tac.1979.1101943

Löfgren, J. S., Haas, R., & Scherneck, H.-G. (2014, October). Sea level time series and ocean tide analysis from multipath signals at five GPS sites in different parts of the world. *Journal of Geodynamics*, *80*, 66–80. Retrieved from `https://doi.org/10.1016/j.jog.2014.02.012` doi: 10.1016/j.jog.2014.02.012

Neumann, B., Vafeidis, A. T., Zimmermann, J., & Nicholls, R. J. (2015, March). Future coastal population growth and exposure to sea-level rise and coastal flooding - a global assessment. *PLOS ONE*, *10*(3), e0118571. Retrieved from `https://doi.org/10.1371/journal.pone.0118571` doi: 10.1371/journal.pone.0118571

Nievinski, F. G., & Larson, K. M. (2013, June). Forward modeling of GPS multipath for near-surface reflectometry and positioning applications. *GPS Solutions*, *18*(2), 309–322. Retrieved from `https://doi.org/10.1007/s10291-013-0331-y` doi: 10.1007/s10291-013-0331-y

Nievinski, F. G., & Larson, K. M. (2014, October). Inverse modeling of GPS multipath for snow depth estimation—part i: Formulation and simulations. *IEEE Transactions on Geoscience and Remote Sensing*, *52*(10), 6555–6563. Retrieved from `https://doi.org/10.1109/tgrs.2013.2297681` doi: 10.1109/tgrs.2013.2297681

NMEA. (2018). *Nmea 0183 interface standard (version 4.11).* Retrieved from `https://www.nmea.org/content/STANDARDS/NMEA_0183_Standard`

Ogaja, C. A. (2022). *Introduction to GNSS geodesy* (1st ed.). Cham, Switzerland: Springer Nature.

Peng, D., Feng, L., Larson, K. M., & Hill, E. M. (2021, October). Measuring coastal absolute sea-level changes using GNSS interferometric reflectometry. *Remote Sensing*, *13*(21), 4319. Retrieved from `https://doi.org/10.3390/rs13214319` doi: 10.3390/rs13214319

Peng, D., Hill, E. M., Li, L., Switzer, A. D., & Larson, K. M. (2019, March). Application of GNSS interferometric reflectometry for detecting storm surges. *GPS Solutions*, *23*(2).

Retrieved from `https://doi.org/10.1007/s10291-019-0838-y` doi: 10.1007/s10291 -019-0838-y

Purnell, D. (2022). *Progress toward a practical gnss-r water level sensor* (Doctoral dissertation, Department of Earth and Planetary Sciences, McGill University, Montreal, Canada). Retrieved from `https://escholarship.mcgill.ca/concern/theses/ th83m470q`

Purnell, D., Gomez, N., Chan, N. H., Strandberg, J., Holland, D. M., & Hobiger, T. (2020). Quantifying the uncertainty in ground-based GNSS-reflectometry sea level measurements. *IEEE Journal of Selected Topics in Applied Earth Observations and Remote Sensing*, *13*, 4419–4428. Retrieved from `https://doi.org/10.1109/ jstars.2020.3010413` doi: 10.1109/jstars.2020.3010413

Roesler, C., & Larson, K. M. (2018, June). Software tools for GNSS interferometric reflectometry (GNSS-IR). *GPS Solutions*, *22*(3). Retrieved from `https://doi.org/ 10.1007/s10291-018-0744-8` doi: 10.1007/s10291-018-0744-8

Santamaría-Gómez, A., & Watson, C. (2016, April). Remote leveling of tide gauges using GNSS reflectometry: case study at spring bay, australia. *GPS Solutions*, *21*(2), 451– 459. Retrieved from `https://doi.org/10.1007/s10291-016-0537-x` doi: 10.1007/ s10291-016-0537-x

Santamaría-Gómez, A., Watson, C., Gravelle, M., King, M., & Wöppelmann, G. (2014, December). Levelling co-located GNSS and tide gauge stations using GNSS reflectometry. *Journal of Geodesy*, *89*(3), 241–258. Retrieved from `https://doi.org/10.1007/ s00190-014-0784-y` doi: 10.1007/s00190-014-0784-y

Strandberg, J. (2020). *New methods and applications for interferometric gnss reflectometry* (Doctoral dissertation, Department of Space, Earth and Environment, Onsala Space Observatory, Chalmers University of Technology, Gothenburg, Sweden). Retrieved from `https://www.proquest.com/dissertations-theses/new -methods-applications-interferometric-gnss/docview/2610039096/se-2`

Strandberg, J., Hobiger, T., & Haas, R. (2016, August). Improving GNSS-r sea level determination through inverse modeling of SNR data. *Radio Science*, *51*(8), 1286–1296. Retrieved from `https://doi.org/10.1002/2016rs006057` doi: 10.1002/2016rs006057

Strandberg, J., Hobiger, T., & Haas, R. (2019, April). Real-time sea-level monitoring using kalman filtering of GNSS-r data. *GPS Solutions*, *23*(3). Retrieved from `https:// doi.org/10.1007/s10291-019-0851-1` doi: 10.1007/s10291-019-0851-1

Tabari, H. (2020, August). Climate change impact on flood and extreme precipitation increases with water availability. *Scientific Reports*, *10*(1). Retrieved from `https://doi.org/10.1038/s41598-020-70816-2` doi: 10.1038/s41598-020-70816-2

Taherkhani, M., Vitousek, S., Barnard, P. L., Frazer, N., Anderson, T. R., & Fletcher, C. H. (2020, April). Sea-level rise exponentially increases coastal flood frequency. *Scientific Reports*, *10*(1). Retrieved from `https://doi.org/10.1038/s41598-020-62188-4` doi: 10.1038/s41598-020-62188-4

Vitousek, S., Barnard, P. L., Fletcher, C. H., Frazer, N., Erikson, L., & Storlazzi, C. D. (2017, May). Doubling of coastal flooding frequency within decades due to sea-level rise. *Scientific Reports*, *7*(1). Retrieved from `https://doi.org/10.1038/s41598-017-01362-7` doi: 10.1038/s41598-017-01362-7

Vu, P.-L., Frappart, F., Darrozes, J., Ha, M.-C., Dinh, T.-B.-H., & Ramillien, G. (2018, July). Comparison of water level changes in the mekong river using gnss reflectometry, satellite altimetry and in-situ tide/river gauges. In *IGARSS 2018 - 2018 IEEE international geoscience and remote sensing symposium.* IEEE. Retrieved from `https://doi.org/10.1109/igarss.2018.8518977` doi: 10.1109/igarss.2018.8518977

Wan, E. A., & van der Merwe, R. (2001, October). The unscented kalman filter. In *Kalman filtering and neural networks* (pp. 221–280). John Wiley & Sons, Inc. Retrieved from `https://doi.org/10.1002/0471221546.ch7` doi: 10.1002/0471221546.ch7

WCRP Global Sea Level Budget Group. (2018, August). Global sea-level budget 1993–present. *Earth System Science Data*, *10*(3), 1551–1590. Retrieved from `https://doi.org/10.5194/essd-10-1551-2018` doi: 10.5194/essd-10-1551-2018

Williams, S. D. P., Bell, P. S., McCann, D. L., Cooke, R., & Sams, C. (2020, October). Demonstrating the potential of low-cost GPS units for the remote measurement of tides and water levels using interferometric reflectometry. *Journal of Atmospheric and Oceanic Technology*, *37*(10), 1925–1935. Retrieved from `https://doi.org/10.1175/jtech-d-20-0063.1` doi: 10.1175/jtech-d-20-0063.1

Xie, S., Chen, J., Dixon, T. H., Weisberg, R. H., & Zumberge, M. A. (2021, November). Offshore sea levels measured with an anchored spar-buoy system using GPS interferometric reflectometry. *Journal of Geophysical Research: Oceans*, *126*(11). Retrieved from `https://doi.org/10.1029/2021jc017734` doi: 10.1029/2021jc017734

Younos, T., & Heyer, C. J. (2015). Advances in water sensor technologies and real-time water monitoring. In *The handbook of environmental chemistry* (pp. 171–203). Springer International Publishing. Retrieved from `https://doi.org/10.1007/978-3-319-14212-8_7` doi: 10.1007/978-3-319-14212-8_7

Appendices

A   Summary Paper

Implementing real-time water level retrieval for GNSS interferometric reflectometry

Alonso Vega-Fernández[1,✉]

[1] Institute of Geodesy and Geoinformation, University of Bonn

Abstract

Real-time water level monitoring enables the fast and precise collection of information that may then be utilized to guide emergency response and decision-making processes. Due to the vulnerability of conventional measurement equipment during extreme events, alternative non-intrusive techniques such as ground-based GNSS Interferometric Reflectometry (GNSS-IR) should be prioritized. For that reason, this thesis aims to develop a real-time GNSS-IR implementation using Ensemble Kalman filter (EnKF) to create a tool compatible with the python package *gnssrefl* capable of monitoring water levels both at the sea surface and in rivers. The results demonstrated that the developed implementation can monitor sea and river levels in real-time using GNSS high-quality devices with RMSE of 4.2 *cm*. The use of low-cost devices was explored in river monitoring, finding that it is possible to obtain RMSE values of 3.0 *cm* or lower when the instrument is installed pointing towards the horizon in the direction of the river.

Introduction

Access to water has historically influenced human settlement patterns and societal systems. Currently, roughly 10% of the world's population lives in coastal areas, which are home to some of the world's largest cities, while another large number has lived in areas near rivers and lakes (1, 2). Thus, numerous human activities and water bodies have a strong interaction, but these settlements are prone to natural calamities and risks. Communities can be warned of potential flood threats and take the required steps to preserve lives and property by monitoring changes in water levels. Remote sensing techniques such as ground-based GNSS Interferometric Reflectometry (GNSS-IR) allow real-time monitoring, providing timely and accurate information, without the need to install measurement instruments in vulnerable areas, which makes it possible to guarantee the tracking of natural disasters (e.g. floods) without losing crucial information that can be used to inform decision-making and emergency response activities.

GNSS-IR is based on the use of multipath effects to deduce the properties of surfaces around the GNSS antenna. The multipath is measured as the Signal-to-noise ratio (SNR), which is a ratio between a signal and a reflected version of it. As shown in Figure 1, the SNR is detected as an interference pattern whose oscillatory part (signal detrended by means of a polynomial of degree 2) stores information from
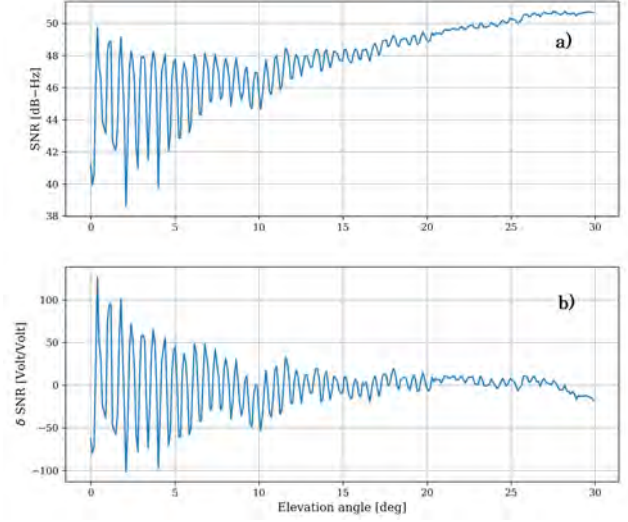
Fig. 1. Placeholder image of Iris with a long example caption to show justification setting.

the reflecting surface. Hence, SNR can be used to deduce the position of the reflective surface.

The most commonly used method for GNSS-RI is the Spectral analysis method which implements the Lomb-Scargle analysis, which studies the oscillating pattern drawn by the SNR to determine the dominant frequency f and uses it to retrieve the height of the reflective surface. Focusing only on the information carried in the detrended oscillating component of the SNR, it can be defined as

$$SNR = A\cos\left(\frac{4\pi h}{\lambda}\sin(\epsilon) + \varphi\right) \tag{1}$$

where A is the amplitude of the oscillations and φ a phase delay caused by surfaces reflective properties (3) . Considering SNR as a sine wave function of $\sin(\epsilon)$, and h constant, the frequency f of the signal can be described by (**?**)

$$f = \frac{2h}{\lambda} \tag{2}$$

For water level, the assumption of a static reflective surface is applicable only when it is relatively stationary during a satellite pass. In the case of a dynamic surface with considerable fluctuations the preceding premise is no longer valid. The retrieved height must be rectified by the change range in this

scenario (4), expressing the frequency by

$$f = \frac{2}{\lambda}\left(h + \frac{\dot{h}\tan(\epsilon)}{\dot{\epsilon}}\right) \qquad \textbf{(3)}$$

where $\dot{h}$ represents the height range of change and $\dot{\epsilon}$ the change in the elevation angle.

An alternative approach for measuring dynamic surfaces is the Least Squares inversion method Strandberg et al. (5). This method builds on the idea of fitting modeled SNR by

$$SNR = A_i \cos\left(\frac{4\pi h(t)}{\lambda_i}\sin(\epsilon) + \varphi\right)e^{-k_i{}^2\Lambda\sin^2(\epsilon)} \qquad \textbf{(4)}$$

where the factor Λ is the damping coefficient that depends on surface properties and antenna gain pattern and accounts for signal attenuation. The subscript i denotes that those parameters are satellite system and transmission frequency dependent (e.g. GPS L1).

However, because the two aforementioned methods require several observations to develop a solution, they are limited to time-delayed solutions. For this reason, the goal of this research is to create a way for using Kalman filtering techniques in conjunction with the inverse modeling approach to retrieve water levels in real time as a tool for GNSS-IR applications.

Current state of Kalman filter approach for GNSS-IR

Focusing on the use of Kalman filters for real-time water level retrieval, which is the main objective of this thesis, we came across the implementation shown by Strandberg et al. (6) for real-time sea level monitoring, in which the use of Unscented Kalman filter (UKF), which is based on the unscented transform (7), was explored as an alternative to deal with highly nonlinear measurement models.

The definition of dynamic height sea level and the state vector in this approach is similar to the one used in the least-squares inversion method. However, due to the nature of the real-time processing, the number of scaling coefficients in the state vector is limited. Therefore, a dynamic update of the state vector was implemented by establishing a time window for a given interval bounded by the scaling coefficients. The results of this study showed that sea level real-time monitoring with GNSS-IR is possible using the UKF and a dynamic B-spline approach.

Kalman filter approach for water-level retrieval

The findings of Strandberg et al. (6) showed that sea level real-time monitoring with GNSS-IR is possible using the UKF and a dynamic B-spline, obtaining water level retrievals with good precision. Nonetheless, the imposition of a B-spline dynamic model can cause the appearance of artifact variations in the water level. Additionally, the UKF has proven to be an easily implemented tool in multiple applications. However, the filter can be unstable depending on the

system noise and measurement noise that are chosen, easily causing the filter to diverge. For this reason, the Ensemble Kalman Filter (EnKF) as presented by Crassidis and Junkins (8) is going to be explored in this thesis as an alternative approach for highly nonlinear models that can be implemented for real-time water retrieval.

The EnKf is a prominent approach in various geoscientific disciplines since it is a Monte Carlo-based version of the KF for very large-dimensional, nonlinear, and non-Gaussian state estimation problems. It is based on the idea that the sample covariance can be used to replace the covariance matrix P in the KF by employing a collection of N state vectors (also called ensembles). Avoiding numerical issues that can occur in trying to maintain and use the state covariance matrix in other KF implementations (8). The samples collection x_t^j with $j = 1, ..., N$ is defined only at the beginning of the implementation and is defined based on an initial state vector x_0 and an initial covariance P_0 as

$$\hat{x}_t^j = \mathcal{N}(x_0, P_0) \qquad \textbf{(5)}$$

The prediction step consists of passing the sample collection through a model to estimate multiple future states of the system. The method can be implemented with a nonlinear system model f so that by

$$\hat{x}_{t|t-1}^j = f(\hat{x}_{t-1|t-1}^j) + w_t^j \qquad \textbf{(6)}$$

where w_t is the zero mean multivariante normal distribution $w \sim \mathcal{N}(0, Q)$, with Q_t as the system noise covariance matrix. The subscript $(t|t-1)$ and $(t-1|t-1)$ denote the predicted and prior states respectively.

The update step occurs at the moment new observations are available, and consists of the use of the Kalman gain K and innovation residuals $\tilde{y}_t^j$ to update the predicted collection of samples by

$$\hat{x}_{t|t}^j = \hat{x}_{t|t-1}^j + K_t\tilde{y}_t^j \qquad \textbf{(7)}$$

where subscript $(t|t)$ denotes that the updated stated corresponds to the current time. The Kalman gain K is computed using

$$K_t = P_t^{xy}(P_t^{yy})^{-1} \qquad \textbf{(8)}$$

where P_t^{yy} is an approximation of the cross-covariance of the modeled observations given by

$$P_t^{yy} = \frac{1}{N-1}\sum_{j=1}^{N}[\hat{y}_t^j - \hat{y}_t][\hat{y}_t^j - \hat{y}_t]^T + R \qquad \textbf{(9)}$$

where $\hat{y}_t$ is the mean of a collection of modeled measurements defined with the predicted states $\hat{x}_{t|t-1}^j$ and the nonlinear measurement model h and given by

$$\hat{y}_t^j = h(\hat{x}_{t|t-1}^j) + v_t \qquad \textbf{(10)}$$

with v_t as the zero mean multivariante normal distribution $v \sim \mathcal{N}(0, R)$, with R_t as the measurements noise covariance matrix. And P_t^{xy} given by

$$P_t^{xy} = \frac{1}{N-1}\sum_{j=1}^{N}[\hat{x}_{t|t-1}^j - \hat{x}_{t|t-1}][\hat{y}_t^j - \hat{y}_t]^T \qquad \textbf{(11)}$$

where $\hat{x}_{t|t-1}$ is the mean of the collection of predicted states. After the update step, the resulting updated state vector $\hat{x}_{t|t}$ is computed as the mean of the states obtained with Equation 7.

The covariance matrix P_t is not needed in the computation of the EnKF. However, it can be approximated using the sample covariance through

$$\hat{P}_t = \frac{1}{N-1} \sum_{j=1}^{N} [\hat{x}_{t|t}^j - \hat{x}_{t|t}][\hat{x}_{t|t}^j - \hat{x}_{t|t}]^T \qquad \textbf{(12)}$$

The elements of the system state vector in the EnKF implementation are n normalized weighting factors W used in the prediction step and the components of the Equation 4, the surface height h, the damping factor Λ, amplitude A, and phase delay φ. The last two parameters are satellite-frequency-specific. Hence, two state vector elements have to be estimated for every satellite system and transmission frequency used. The height and the damping factor are shared by all reflected signals, so each adds only one element to the state vector. The total number of state vector elements M is given by

$$M = n + 2M_f + 2 \qquad \textbf{(13)}$$

The initial state vector x_0 elements were defined with the δSNR from 24 hours previous. The initial height h is estimated by using the LSP method, the initial amplitude A can be estimated as the value of 3σ of the δSNR, and the phase delay φ can be initialized as a small value (e.g. $0.01\ rad$). Finally, good guesses of the damping factor Λ were empirically defined as 0.1.

The initial covariance matrix P_0 is needed to define the sample collection of the EnKF. The initial values were defined as high variances so that the sample spreads out around the initial values and allows the filter to converge towards the best estimates of the state of the system. The weighting factors W are initialized with 0 variances.

Once the filter is started, the prediction step is defined to

$$\hat{x}_{t|t-1} = \hat{x}_{t-1|t-1} + \sum_{i=1}^{n} W_i \Delta h_{t-i} + w_t \qquad \textbf{(14)}$$

where the best prediction of the future state $\hat{x}_{t|t-1}$ is the previous state $\hat{x}_{t-t|t-1}$ plus a weighted moving average of the height changes δh_{t-i} determined in n^{th} previous times, multiply by the weighting factors W_i, plus the process noise w_t that accounts for the possible error in the prediction step.

At the beginning of the implementation, the weighting factors are estimated as

$$W_i = \frac{1}{\Delta t^i}$$

where Δt is the sample rate of the SNR used in the implementation. And normalized so that $\sum_{i=1}^{n} W_i = 1$. Subsequently, the nth power factors are added to the state vector so that the filter takes care of updating them based on the evolution of the data.

Under normal conditions, no significant changes are expected in water level in short periods of time. Likewise, as was explained by Strandberg et al. (5), the other state elements can be considered to be slowly variable even in long periods of time (e.g. days) and affected in part by surface conditions that are difficult to predict. Therefore, in this implementation, all these external factors are considered constant and their changes as random processes defined by small process noises, allowing the elements of the state vector to change during the update process if the residuals are improved.

The process noises determine how well the EnKF implementation will estimate the water level and the other parameters of the system state. As the real water level dynamic is site-specific and also depends on external factors, the right process noise is difficult to be defined. In this study, the process noise for every tested site was empirically established to guarantee a stable solution under the site conditions at the moment the data was measured. The same process noise was defined for all amplitude and phase delay parameters. In the case of the weighting parameters, a small system noise of $1x10^{-11}$ is added to allow the filter to add small updates to the factors. In the update step, as the real measurement noise is unknown, is defined as the variance of the δSNR.

The real-time solution performance is evaluated by comparing the results along with tide or river gauges time series by using RMSE, which is a common way to estimate how predicted values match up to observed values by

$$RMSE = \sqrt{\frac{\sum_{j=1}^{N} (X_{pred_j} - X_{obs_j})^2}{N}} \qquad \textbf{(15)}$$

where X_{pred} and X_{obs} are vectors of N the predicted and observed values respectively.

Results and Discussion

The resulting real-time water level estimations were evaluated by comparing them to co-located tide or river gauges water level series. Two coastal sites (TGMX and CALC) were used to assess the real-time sea level monitoring and the detection of storm surges, while real-time river level monitoring and river flood detection were evaluated in three river bank sites (GWES, WESL, and BEUE). At the same time, in the river bank sites (WESL and BEUE), it is explored the use of low-cost antenna data as a data source for river level monitoring in real-time.

Both TGMX and CALC are sites with GNSS stations that records GPS, GLONASS, and Galileo in time intervals of 15 seconds and have a clear line of sight in the direction of the sea surface. The TGMX site has a reflection zone that covers 160° between its azimuthal limits (almost 50% of available data). In terms of the elevation angles, data in the range of 4° to 20° were used. The CALC site has a reflecting zone with azimut limits of 190° to 340°, while the elevation angles include angles between 4° to 25°.

In TGMX, the estimation was computed from February 12th to March 14th, 2022, using all the available observations.
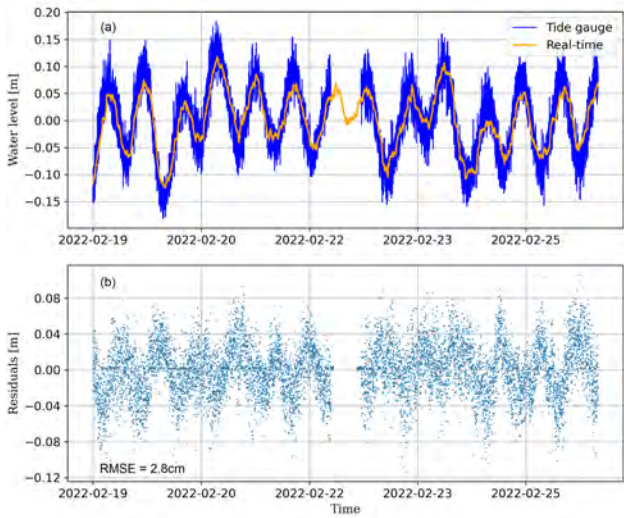
Fig. 2. Placeholder image of Iris with a long example caption to show justification setting.
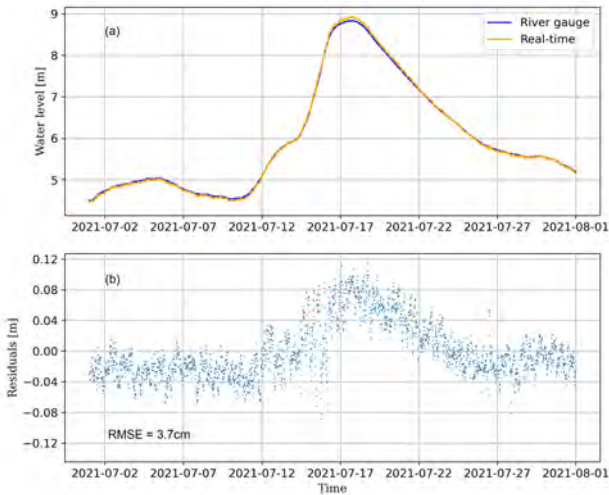

Fig. 3. Placeholder image of Iris with a long example caption to show justification setting.

The implementation was run using SNR data with a frequency of 15 and 30 seconds. A subset of seven days of the tide gauge records and real-time GNSS-IR solution is presented in Figure 2 (a). As a result, the real-time solution showed a RMSE of 2.8 cm. The same result was obtained when using 15 and 30 seconds data. This is because the change in sea level that occurs in both time intervals is equivalent. The residuals (Figure 2 (b)) showed a good performance of the real-time solution. The high-frequency variation noticed in the tide gauge time series is due to the fact that the radar sensor is installed outdoors and its measurements are affected by near-shore waves.

In CALC, the estimation was computed from November 22th to December 10th, 2022, using all the available observations. The GNSS-IR real-time solution using both frequency rate data showed a RMSE of 4.2 cm.

The usefulness of the real-time implementation was proved for storm surge observation with data collected at the site CALC in 2017 and 2020. Between August 25th and 29th, 2017, Hurricane Harvey moved through the area of the Gulf of Mexico generating storm surges that hit where CALC is located. While in the period from August 26th to August 28th, 2020, Hurricane Laura passed directly over the CALC site. Allowing the influence of these atmospheric phenomena on the sea level to be measured on both occasions. And it was found a good performance obtaining a RMSE of 4.4 cm monitoring storm surges, the same precision achieved at that site when monitoring sea level under normal conditions. However, it was determined that when the winds caused by the hurricane reached speeds higher than 30 m/s there is an increase in the roughness of the water surface as a consequence of the increasing significant wave height that decreases the specular reflection to the point in which the filter is not able to assimilate the water surface changes.

The real-time river level determination with GNSS-IR was explored to assess the capability of the implementation to retrieve river levels, but it also focused on the monitoring of level increases that can cause flooding.

The study was conducted on the site GWES from July 1st to July 31st, 2021, using all the available observations (e.i. GPS, GLONASS, and Galileo) with an observations frequency of 30 seconds. The period of time studied is relevant because, during it, significant rainfall drastically increased the level of various bodies of water, inducing flood events. In the case of the Rhine, the river level rose by more than 4.9 m. The reflection zone was delimited to the azimuth interval 260° to 320° and the elevation angles from 5° to 15°. This small size of the reflection zone results in multiple intervals of up to 90 minutes with no measurements in which the filter cannot update the state vector. Nevertheless, the final result demonstrated that the filter estimation was capable of accurately drawing the level changes before, during, and after the rise of the river level (see Figure 3 (a)). Obtaining a RMSE of 3.7 cm.

Based on the good performance obtained using high-quality GNSS antennas, it is appropriate to examine if it is possible to use observations obtained with low-cost GPS devices for the real-time monitoring of rivers.

A PRP instrument (9) was installed in the sites WESL and BEUE in different epochs. In both test sites GPS L1 observations were recorded in time intervals of 1 second (1 Hz). However, the SNR data rate was decimated at 30 seconds in order to match the results with what has been previously obtained using more sophisticated GNSS antennas. The WESL site shares location with GWES. Therefore, both have a similar line of sight to the river surface, with the same limitations.

During its operation in WESL, the PRP instrument was used in two different orientation setups. At first, the GPS antenna was installed in the zenith orientation position, while in the second orientation set-up, the antenna was tilted 90° from the vertical direction toward the river. For this reason, the use of real-time implementation was studied using both data sets separately. The first part of the study was conducted from July 1st to July 31st, 2021. In this period, the GPS antenna

was installed in the zenith orientation position.

The estimations showed poor results, in which the filter was not able to follow the variation of the river level accurately with a RMSE of 43.3 cm. For comparison, the data obtained by GWES were processed again but used only the GPS L1 signal yielding results with an RMSE of 5.6 cm. However, when implementation was tested from September 21st to October 21st, 2021. With the instrument pointing toward the river, the real-time river level solution was determined with a RMSE of 3.0 cm. Therefore, the difference between the results must be mainly related to the capability of each device to measure satellite signals accurately.

The same GPS antenna was used at the BEUE site. The PRP instrument was installed pointing toward the river. The reflection zone at BEUE was limited to an azimuthal range of $140°$ to $280°$ and elevation angles of $3°$ to $20°$, implying that the area across which reflections can be perceived is more than twice as wide as the total area available at the WESL site. The implementation was tested from November 2nd to November 15^{ht}, 2022, obtaining a real-time river level solution with a RMSE of 1.9 cm.

Conclusions

With these results, it is feasible to deduce that real-time monitoring of river levels is conceivable using low-cost devices like the PRP instrument when installed so that it points towards the horizon and the water surface. This orientation setup enables the accuracy of the results acquired to be equivalent to that of considerably more complex and expensive geodetic antennas.

The Ensemble Kalman Filter (EnKF) was used to build a real-time GNSS-IR water level monitoring system. The implementation was tested in the estimation of the sea level variation by using data obtained by GNSS antennas capable of measuring data from multiple satellite constellations and signals with a measurement rate of 15 and 30 seconds in two different sites. The results showed that the implementation developed in this thesis is capable of monitoring the sea level in sites with moderate tides with a good performance following the dynamics of the ocean with differences between the estimated water height and the reference value is less than 5 cm in more than 90% of the cases, and nearly 100% less than 10 cm. Overall, an RMSE of less than 4.2 cm was achieved. This demonstrates the potential of the developed implementation. In river monitoring, the real-time implementation has shown good performance in monitoring river level variations, including the measurement of flood occurrences, with an RMSE of 3.7 cm, evidencing the high accuracy of the water levels estimated by the filter, and demonstrating that real-time river level monitoring can be determined with precision comparable to that obtained with river pressure gauges.

The usage of real-time implementation for storm surge monitoring provided evidence that variations in water surface roughness can be assimilated by the filter to the point where extreme storm winds minimize the specular reflections by substantially increasing the significant wave height. Therefore, it is appropriate to consider the use of the models applied in the estimation of the significant wave height by means of GNSS-IR as an alternative to improve the performance of the real-time implementation under the previously mentioned challenging conditions.

Results using data from devices that only measure GPS signals at the L1 frequency showed that when the low-cost antenna was tilted $90°$ to the vertical, excellent performance was attained with RMSE of 3.0 cm. Demonstrating that results comparable to those obtained using data acquired by more expensive and higher-quality antennas can be achieved. These results support the use of low-cost devices as an alternative to monitoring water surfaces with non-intrusive techniques. Exploring the use of low-cost devices capable of measuring multiple constellations and signals is an alternative for future work to test the accuracy of the solution in real-time monitoring of sea and river levels.

Bibliography

1. Barbara Neumann, Athanasios T. Vafeidis, Juliane Zimmermann, and Robert J. Nicholls. Future coastal population growth and exposure to sea-level rise and coastal flooding - a global assessment. *PLOS ONE*, 10(3):e0118571, March 2015. doi: 10.1371/journal.pone.0118571.

2. Ebru Kirezci, Ian R. Young, Roshanka Ranasinghe, Sanne Muis, Robert J. Nicholls, Daniel Lincke, and Jochen Hinkel. Projections of global-scale extreme sea levels and resulting episodic coastal flooding over the 21st century. *Scientific Reports*, 10(1), July 2020. doi: 10.1038/s41598-020-67736-6.

3. Felipe G. Nievinski and Kristine M. Larson. Forward modeling of GPS multipath for near-surface reflectometry and positioning applications. *GPS Solutions*, 18(2):309–322, June 2013. doi: 10.1007/s10291-013-0331-y.

4. K. M. Larson, R. D. Ray, F. G. Nievinski, and J. T. Freymueller. The accidental tide gauge: A GPS reflection case study from kachemak bay, alaska. *IEEE Geoscience and Remote Sensing Letters*, 10(5):1200–1204, September 2013. doi: 10.1109/lgrs.2012.2236075.

5. Joakim Strandberg, Thomas Hobiger, and Rüdiger Haas. Improving GNSS-r sea level determination through inverse modeling of SNR data. *Radio Science*, 51(8):1286–1296, August 2016. doi: 10.1002/2016rs006057.

6. Joakim Strandberg, Thomas Hobiger, and Rüdiger Haas. Real-time sea-level monitoring using kalman filtering of GNSS-r data. *GPS Solutions*, 23(3), April 2019. doi: 10.1007/s10291-019-0851-1.

7. Simon J. Julier and Jeffrey K. Uhlmann. New extension of the kalman filter to nonlinear systems. In Ivan Kadar, editor, *SPIE Proceedings*. SPIE, July 1997. doi: 10.1117/12.280797.

8. John L Crassidis and John L Junkins. *Optimal estimation of dynamic systems, second edition*. Chapman & Hall/CRC Applied Mathematics & Nonlinear Science. Chapman & Hall/CRC, Philadelphia, PA, 2 edition, October 2011. ISBN 978-1-4398-3986-7.

9. Makan A. Karegar, Jürgen Kusche, Felipe Geremia-Nievinski, and Kristine M. Larson. Raspberry pi reflector (RPR): A low-cost water-level monitoring system based on GNSS interferometric reflectometry. *Water Resources Research*, 58(12), November 2022. doi: 10.1029/2021wr031713.

B   Poster

Implementing real-time water level retrieval for GNSS interferometric reflectometry
Master thesis submitted by Alonso Vega-Fernández

Abstract

Real-time water level monitoring enables the fast and precise collection of information that may then be utilized to guide emergency response and decision-making processes. Due to the vulnerability of conventional measurement equipment during extreme events, alternative non-intrusive techniques such as ground-based GNSS Interferometric Reflectometry (GNSS-IR) should be prioritized. For that reason, this thesis aims to develop a real-time GNSS-IR implementation using Ensemble Kalman filter (EnKF) to create a tool compatible with the python package *gnssrefl* capable of monitoring water levels both at the sea surface and in rivers. The results demonstrated that the developed implementation can monitor sea and river levels in real-time using GNSS high-quality devices with RMSE of 4.2 *cm*. The use of low-cost devices was explored in river monitoring, finding that it is possible to obtain RMSE values of 3.0 *cm* or lower when the instrument is installed pointing towards the horizon in the direction of the river.

Study area

Fig. 1. Test site TGMX. (a) Mask, azimuth: 30°–190° and elevation angle: 4°-20°. (b) Location.

Fig. 2. Test site CALC. (a) Mask, azimuth: 190°–340° and elevation angle 4°-25°. (b) Location.

Fig. 3. Test site WESL. (a) Mask, azimuth: 260°–320° and elevation angle: 5°-15°. (b) Location.

Fig. 4. Test site BEUE. (a) Mask, azimuth: 140°–280° and elevation angle 3°-20°. (b) Location.

Real-time implementation

► The Ensemble Kalman filter (EnKF) was implemented to create a tool compatible with the python package *gnssrefl* capable of monitoring water levels both at the sea surface and in rivers.

► The prediction of the state was enhanced by taking into account the height changes of *n* instates towards the past, assigning weights so that the changes closer to the present have greater weight.

► The measurement model is based on the function of the SNR inverse modeling method.

$$SNR = A_i \cos\left(\frac{4\pi h(t)}{\lambda_i}\sin(\epsilon) + \varphi\right) e^{-k_i{}^2 \Lambda \sin^2(\epsilon)} \quad (1)$$

► Observations are *SNR* values measured using GNSS antennas measuring multiple satellite constellations and frequencies. In addition to low-cost devices that only measure GPS L1.

► The filter solutions were compared with measurements from tide gauges and river gauges to estimate the precision of the result by

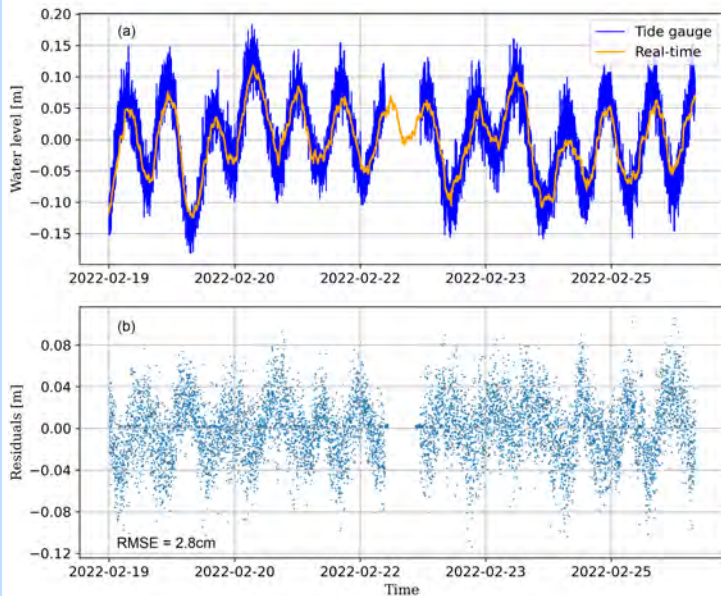$$RMSE = \sqrt{\frac{\sum_{j=1}^{N}(X_{pred_j} - X_{obs_j})^2}{N}} \quad (2)$$

Results

Fig. 5. (a) Sea level estimation, TGMX. (b) Residuals

Fig. 5. (a) River level estimation, GWES. (b) Residuals

The developed implementation can monitor sea level in real-time using measurements that capture multiple constellations and frequencies with RMSE of 4.2 *cm*. However, the performance of the filter was limited when facing extreme conditions where the surface roughness ban specular reflections. River level in real-time was determined with RMSE of 3.7 *cm*. The use of low-cost devices showed that it is possible to obtain RMSE values of 3.0 *cm* or less when the instrument is installed pointing towards the horizon in the direction of the river.
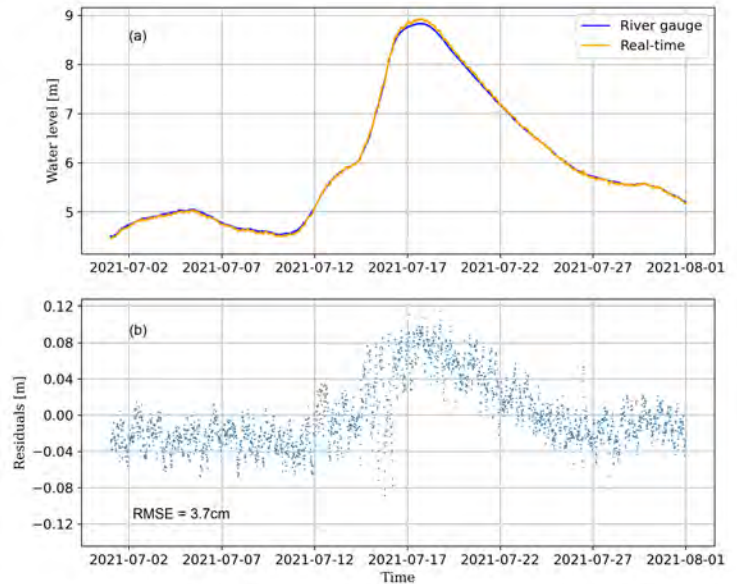
Conclusion

Real-time GNSS-IR water level monitoring of both inland and coastal waters is possible with the EnKF implementation using 15 and 30 second data. Obtaining RMSE less than 5.0 cm when using data from GNSS devices.

Low-cost devices that measure only GPS L1 signals are promising for real-time river level monitoring when installed by tilting the antenna 90° from the vertical direction toward the river.

Literatur

JOHN L CRASSIDIS AND JOHN L JUNKINS. OPTIMAL ESTIMATION OF DYNAMIC SYSTEMS, SECOND EDITION. CHAPMAN HALL/CRC APPLIED MATHEMATICS NONLINEAR SCIENCE. CHAPMAN HALL/CRC, PHILADELPHIA, PA, 2 EDITION, OCTOBER 2011. ISBN 978-1-4398-3986-7. FELIPE G. NIEVINSKI AND KRISTINE M. LARSON. FORWARD MODELING OF GPS MULTIPATH FOR NEAR-SURFACE REFLECTOMETRY AND POSITIONING APPLICATIONS. GPS SOLUTIONS, 18(2):309–322, JUNE 2013. DOI: 10.1007/s10291-013-0331-y. MAKAN A. KAREGAR, JÜRGEN KUSCHE, FELIPE GEREMIA-NIEVINSKI, AND KRISTINE M. LARSON. RASPBERRY PI REFLECTOR (RPR): A LOW-COST WATER-LEVEL MONITORING SYSTEM BASED ON GNSS INTERFEROMETRIC REFLECTOMETRY. WATER RESOURCES RESEARCH, 58(12), NOVEMBER 2022. DOI:10.1029/2021wr031713.

Institut für Geodäsie und Geoinformation
Professur für Astronomische, Physikalische und Mathematische Geodäsie
Nussallee 17, 53115 Bonn